

This is the final peer-reviewed accepted manuscript of:

Gaete Rojas, A., Kavanagh, J. L., Rivalta, E., Hilmi Hazim, S., Walter, T. R., Dennis, D. J. C. (2019): The impact of unloading stresses on post-caldera magma intrusions. - Earth and Planetary Science Letters, 508, pp. 109—121.

The final published version is available online at:  
<http://doi.org/10.1016/j.epsl.2018.12.016>

Rights / License:

The terms and conditions for the reuse of this version of the manuscript are specified in the publishing policy. For all terms of use and more information see the publisher's website.

*This item was downloaded from IRIS Università di Bologna (<https://cris.unibo.it/>)*

***When citing, please refer to the published version.***

1 **The impact of unloading stresses on post-caldera magma intrusions**

2 Ayleen Gaete<sup>1</sup>, Janine L. Kavanagh<sup>2</sup>, Eleonora Rivalta<sup>1</sup>, Suraya Hilmi Hazim<sup>2</sup>, Thomas R.  
3 Walter<sup>1</sup>, David J.C. Dennis<sup>3</sup>

4 <sup>1</sup> GFZ German Research Centre for Geosciences, Telegrafenberg, 14473 Potsdam, Germany

5 <sup>2</sup> Department of Earth, Ocean and Ecological Sciences, University of Liverpool, Jane Herdman  
6 Laboratories, Liverpool L69 3GP, UK.

7 <sup>3</sup> School of Engineering, University of Liverpool, Liverpool L69 3GH

8 Corresponding author: Ayleen Gaete (agaete@gfz-potsdam.de)

9 **Abstract**

10 Calderas represent morphological depressions several kilometers in diameter, and the  
11 unloaded crustal stresses they produce can form rapidly (e.g. Pinatubo, 1990) or slowly (e.g.  
12 Hawaii, 2018). Active calderas are known as sites of persistent magma intrusions, and yet the  
13 dynamics of their shallow plumbing system is not well constrained. We use scaled laboratory  
14 experiments to study how experimental intrusions are created beneath a caldera by injecting  
15 dyed water (magma analogue) into the base of an elastic gelatin solid (crust analogue) with a  
16 cylindrical cavity in its surface to mimic a caldera-like topography. The evolving dike geometry  
17 and stress field were qualitatively determined using polarized light, and digital image  
18 correlation allowed the incremental and total strain to be quantified by tracking passive-tracer  
19 particles in the gelatin that fluoresced in a thin 2D vertical laser sheet. Our results show that  
20 the unloaded stress field from a caldera can cause a divergence of vertical dikes, and leads to  
21 circumferential dikes and cone sheets. When the caldera was large the initially vertical dike  
22 became arrested, then grew laterally via circumferentially-propagating en echelon segments;  
23 these eventually joined to complete a cone sheet that was parallel to, but extended outside  
24 and beneath, the large caldera. When the caldera was small, a circumferential dike erupted,  
25 producing a short fissure which was outside, but parallel to, the caldera. We suggest that the  
26 distinct curved geometry, velocity, strain and stress characteristics of circumferential dikes  
27 and cone sheets can be used to interpret the origin and growth of post-caldera magmatism  
28 and the likelihood of eruption in caldera systems.

29 **Keywords:** Caldera, cone sheet, gelatin analogue modeling, circumferential dike, digital  
30 image correlation

31 **Highlights**

- 32 • Circumferential dike and cone sheet dynamics are modeled
- 33 • Unloaded stress (caldera) affects intrusion geometry, velocity, strain and stress
- 34 • Early stages of circumferential dike and cone sheet growth are identical
- 35 • Cone sheets grow laterally at depth via en echelon arcuate segments

36 **1. Introduction**

37 Calderas are associated with some of the largest volcanic systems (e.g. Yellowstone, USA)  
38 where topographic lows form due to subsidence along caldera ring faults (Cole et al., 2005).  
39 Caldera-forming events can be rapid (Mt Pinatubo in Philippines, 1990, e.g. Pallister et al.,  
40 1996) or slow (Kilauea volcano in Hawaii, 2018, e.g. USGS, 2018) and may form due to  
41 explosive volcanic eruptions (Cole et al., 2005) or gradual drainage of a deep reservoir by  
42 lateral intrusion. Despite the largest cataclysmic eruptions being produced during the  
43 formation of the caldera itself (Jellinek and DePaolo, 2003), unrest at calderas and relatively  
44 small post-caldera eruptions are frequent and pose a significant hazard to the population.  
45 Caldera systems are active sites of mineralization, and understanding their development and  
46 impact on the volcanic plumbing system is important for georesources, e.g. copper-porphyry  
47 deposits (e.g. Blundy et al., 2015), and carbonatite-hosted Rare Earth Elements (e.g. Le Bas,  
48 1987). Irregular topographies and crustal loads are common in volcanic terrains, from tectonic  
49 rift zones (e.g. Afar and Iceland) to laterally collapsed sectors of a volcanic edifice (e.g. Mt St  
50 Helens, USA), unstable volcanic islands (e.g. La Palma, Canary Islands), ice unloading, and  
51 excavation of quasi-cylindrical craters associated with volcanic vents, calderas, tuff cones and  
52 diatremes.

53 Field observations suggest that post-caldera magmatism typically occurs via inclined sheet  
54 intrusions (Burchardt et al., 2011). These may take a variety of forms (e.g. Burchardt et al.,  
55 2018). In this paper we use the terms ‘circumferential dike’, which have an arcuate horizontal  
56 section, and ‘cone sheet’, which taper downwards towards a central point and have a circular  
57 horizontal section, to distinguish and reflect the end member intrusion geometries, without  
58 reference to their process of formation. These intrusion types are common igneous magma

59 bodies, are a major constituent of sub-volcanic plumbing systems, and may feed eruptions in  
60 caldera settings (e.g. Bagnardi et al., 2013; Chadwick et al., 2011).

61 There are several contrasting conceptual models to explain cone sheet formation, but these  
62 often do not invoke the presence of a caldera. For example, Galland et al. (2014) carried out  
63 an experimental study of cone sheet development by injecting oil into compacted silica flour  
64 with a flat topography. They found that cone sheets formed due to a dynamic dimensionless  
65 ratio which included the effects of magma viscosity and host-rock deformation mode. In  
66 comparison, Magee et al. (2012) proposed that cone sheets form by lateral propagation of  
67 regional dikes from an adjacent source, whereas other authors invoke stress changes from a  
68 central magma chamber at depth (Anderson, 1936; Geshi, 2005; Johnson et al., 1999; Schirnick  
69 et al., 1999). These fundamentally different models demonstrate there remains uncertainty in  
70 the growth dynamics of the magmatic system, and cone sheets in particular. Accurately  
71 interpreting the surface signals of magma movement for hazard assessment at active  
72 volcanoes ultimately depends on the quality of the models upon which these inferences are  
73 made (Di Vito et al., 2016; Guldstrand et al., 2017).

74 The emplacement, propagation and geometry of magma intrusions are influenced by several  
75 related factors including density contrasts between magma and host-rock, the ambient stress  
76 field (tectonic, regional or local), stress barriers, the physical properties of the intruding  
77 magma (e.g. viscosity), and mechanical heterogeneities in the crust such as rock layering and  
78 faults (see reviews by Burchardt et al., 2018 and; Rivalta et al., 2015). A commonly explored  
79 scenario is that of dike propagation beneath a volcanic edifice where crustal loading influences  
80 the tendency for magma to stall at depth or erupt, and whether an eruption occurs in the  
81 summit or flank of the volcano (Kervyn et al., 2009; Maccaferri et al., 2011), depending on the  
82 magma buoyancy, edifice size and crustal layering (density, rigidity and interface weakness).

83 The load from a volcanic edifice can cause the attraction of dikes located away from the  
84 volcano, and in some cases promote their lateral (blade-like) propagation rather than vertical  
85 growth (Watanabe et al., 2002). This supports the hypothesis that dikes change their  
86 trajectory during propagation in response to perturbations of the maximum compressive  
87 stress ( $\sigma_1$ ), whose orientation may vary due to local or regional compression or extension of  
88 the medium (Anderson, 1936; Maccaferri et al., 2011; Mathieu et al., 2015; Rivalta et al.,  
89 2015).

90 Magma propagation under a topographic low, such as a caldera, has been relatively  
91 unexplored, despite such unloaded stress fields being common features in volcanic terrains  
92 (Corbi et al., 2015; Mathieu et al., 2008). Numerical and analogue modeling suggest that a  
93 caldera geometry in a volcanic edifice induces unloading stresses that in a cohesive, crystalline  
94 rock may favor the emplacement of laminar intrusions with circumferential and/or radial  
95 shapes and sills (Corbi et al., 2016, 2015).

96 Despite the significance of post-caldera magmatism, questions remain regarding the nature  
97 of magma intrusion in an unloaded crust. We present results from gelatin laboratory  
98 experiments that model the emplacement of a dike in the vicinity of a caldera-like topography.  
99 The experiments integrate measurements of sub-surface strain evolution and stress evolution  
100 using digital image correlation and polarized light, respectively. Our results test existing  
101 models of circumferential dike and cone sheet development and assist in their interpretation  
102 by constraining their geometry, propagation pathway, sub-surface deformation and likelihood  
103 of eruption.

## 104 **2. Modeling Framework**

### 105 **2.1. Scaling and selection of analogue materials**

106 Following the approach described by Merle (2015), we define a laboratory prototype scaled  
107 geometrically (ratio of distances is constant in nature and the prototype), kinematically (the  
108 geometric scaling is maintained over time), and dynamically (the ratio of the mechanical forces  
109 between nature and the model is constant). Our selected analogue material for the crust is  
110 gelatin, and for magma we have selected water (see Supplementary Table S1 for detailed  
111 scaling). Gelatin has been very well studied in scaled laboratory experiments to simulate  
112 elastic process in the crust associated with magmatic intrusions (Di Giuseppe et al., 2009;  
113 Kavanagh et al., 2013). Gelatin is a visco-elastic material and its transparency allows the  
114 evolving dynamic process of dike propagation to be visually tracked in an experiment (Takada,  
115 1990; Watanabe et al., 2002). When used at low concentration (2-5 wt.%) and at low  
116 temperature (5-10 °C) it behaves elastically over the timescale of an experiment (Kavanagh et  
117 al., 2013), which lasts approximately 10 minutes. Gelatin has been intruded by a range of fluids  
118 to simulate dike emplacement (see Janine L Kavanagh et al., 2018 for a review). We have  
119 chosen water as the magma analogue as it is a low-viscosity fluid ( $10^{-3}$  Pa s) and is slightly less  
120 dense than the gelatin ( $\Delta\rho = 6 \text{ kgm}^{-3}$ ). It is a suitable analogue to simulate intrusions of low to  
121 intermediate viscosity magma that is mostly driven by the overpressure of liquid from a  
122 distant source (Kervyn et al., 2009), and it has been used in several previous experiments that  
123 study dike propagation (Kavanagh et al., 2018; McLeod and Tait, 1999).

124 We define the geometric scale between nature  $n$  and prototype  $p$  in our experiments as the  
125 length scale factor:

$$126 \quad L^* = \frac{L_p}{L_n} \quad [1]$$

127 Giving  $L^* = 1.0 \times 10^{-5}$  such that 1 cm in the laboratory represents 1 km in nature, considering  
128 that in nature the size of calderas range from 1 km to tens of kilometers in diameter (see Table



129 S1). An alternative length scale factor is the buoyancy length  $L_b$  when magma buoyancy drives  
 130 the rock fracture (Corbi et al., 2016; Kavanagh et al., 2013; Merle, 2015):

$$131 \quad L_b^* = \left( \frac{K_c}{\pi^2 \Delta \rho g} \right)^{\frac{2}{3}} \quad [2]$$

132 where  $K_c$  is the fracture toughness of the host medium,  $\Delta \rho$  is the density contrast between  
 133 host rock and magma, and  $g$  is gravity (Taisne and Tait, 2009). Therefore we calculate  $L_b^* =$   
 134  $4.1 \times 10^{-5}$  (see Table S1). Overall, the two length scales (Equations 1 and 2) agree as they are  
 135 within the same order of magnitude.

136 We have used two contrasting approaches to scale the stresses in our experiments: firstly we  
 137 scale the elastic deformation of the host material, and secondly we scale the unloading  
 138 pressure associated with the caldera. Firstly, we calculate the strain scale factor  $e^*$ :

$$139 \quad e^* = \frac{a}{b} \quad [3]$$

140 where  $a$  is the dike thickness and  $b$  is the dike width. This means  $e^* = 10$  when  $e_n = 0.002$   
 141 and  $e_p = 0.02$  in gelatin (Kavanagh et al., 2013). We define a Young's modulus scale factor  
 142  $E^* = 3 \times 10^{-7}$ , as  $E_n = 10^9 - 10^{10}$  (Kavanagh et al., 2013) and  $E_p = 300 - 3000$  (see Table  
 143 S1). As the elastic deformation of the gelatin can be defined by the relationship between stress  
 144 ( $\sigma$ ), strain ( $e$ ) and Young's modulus ( $E$ ) (Gudmundsson, 2006; Merle, 2015):

$$145 \quad \sigma^* = E^* e^* \quad [4]$$

146 This gives  $\sigma^* = 3.0 \times 10^{-6}$  (see Table S1). We also use the unloading pressure scale factor:

$$147 \quad \sigma^* = P_U^* = \rho_r^* g^* D^* \quad [5]$$

148 where  $D$  is the caldera depth and  $\rho_r$  is the host rock density. As  $\rho_r^* = 0.37$  and  $D^* = 1 \times$   
 149  $10^{-5}$ , this gives  $\sigma^* = 3.7 \times 10^{-6}$ . The agreement between the stress values calculated from  
 150 both of these approaches (Equation 4 and 5) confirms that we have properly scaled our  
 151 experiments.

152 **3. Experimental methodology**

153 **3.1. Gelatin Preparation and Young's modulus measurement**

154 We use pigskin gelatin solids (20 Mesh, 260 Bloom; supplied by Gelita UK) prepared at 2.5  
155 wt.% by dissolving the appropriate amount of gelatin powder into water at 80°C. The mixture  
156 preparation requires three stages: an initial stage where a concentrated mixture is created  
157 and left to cool until it reaches ~ 30°C, then the remaining water is added at 5°C to achieve a  
158 mixture temperature of ~23°C. Some experiments required the addition of passive-tracer  
159 particles, coated in Rhodamine-B which fluoresces in laser light, to the liquid gelatin in order  
160 to apply Digital Image Correlation (DIC) analysis (Sutton et al., 1983). For this purpose, 20-50  
161 µm diameter fluorescent particles (peak fluorescence wavelength: 590 nm) are added to the  
162 gelatin mixture following the method described by Kavanagh et al. (2015). A clear-Perspex  
163 tank (40 cm square-base, 30 cm high; Figure 1) is then filled up to 23 cm height and the mixture  
164 stirred until it reaches the gel point (21°C) to obtain a homogeneous distribution of particles  
165 in the solid gel. A caldera-like geometry is established using a round, plastic container (9 or 12  
166 cm diameter) placed onto the gelatin surface and fixed into position relative to the central  
167 injection port in the base of the experimental tank using plastic tape. The depth of the caldera  
168 is controlled by adding water to the plastic container so that it is submerged by 4 cm depth.  
169 Subsequently, the gelatin mixture is covered with vegetable oil which is carefully poured onto  
170 its surface to inhibit dehydration, the tank is then covered with plastic wrapping and then left  
171 to cool and solidify in a refrigerator set at 5°C for 20 hours. The tank is then taken from the  
172 refrigerator, and the plastic container is removed from the center of the gelatin solid by filling  
173 it with hot water to allow an easy release and avoid any damage at the floor and/or wall of  
174 the caldera that is formed. The oil is then carefully removed using a spoon and paper towel,  
175 and the actual depth of the caldera is measured (typically 3-4 cm, see Table 1).

176 Immediately prior to the experiment starting, the Young's Modulus of the gelatin is calculated  
177 by measuring the deflection to the gelatin surface caused by two cylindrical brass loads placed  
178 sequentially on the gelatin slab (see Supplementary Table S2 for load properties). The load is  
179 placed away from the corner of the tank to minimize any wall effects. The Young's Modulus  
180 is calculated using the following equation (Kavanagh et al., 2013):

$$181 \quad E = \frac{mg(1-\nu^2)}{\Psi w} \quad [6]$$

182 where  $m$  is the load mass,  $g$  is the acceleration due to gravity,  $\nu$  is the Poisson's ratio (0.5 for  
183 gelatin (e.g. Kavanagh et al., 2013; Watanabe et al., 2002)),  $\Psi$  is the load diameter, and  $w$  is  
184 the deflection of the surface produced by the load. The average Young's modulus from each  
185 load placement is then reported (see Table 1).

## 186 **3.2. Experiment Setup**

187 Two imaging techniques were used on the experiments to study the subsurface processes  
188 associated with dike growth and evolution using two different sets of apparatus:  
189 photoelasticity for visualizing stress (Figure 1A), and tracer particle for measuring sub-surface  
190 strain and displacement (Figure 1B). To create an experimental dike, a small cut is made in the  
191 bottom of the gelatin slab, which controls the orientation of the initial dike. A metal pipe with  
192 a tapered end is inserted into this slit and dyed water is injected using a peristaltic pump at a  
193 constant volumetric flow rate ( $Q$ ) of  $3.9 \times 10^{-7} \text{ m}^3/\text{s}$ . The fluid velocity ( $V$ ) is approximated by  
194 dividing  $Q$  by the cross-sectional area of the 1 mm-diameter injection outlet. Injections were  
195 made at two different offset positions (0.0 cm and 1.0 cm, relative to the center of the caldera)  
196 beneath two different caldera sizes (see Table 1).

### 197 **3.2.1. Photoelasticity setup**

198 Polarized light is known to be a useful tool to visualize the stress distribution in two  
199 dimensional elastic problems (Crisp, 1952; Watanabe et al., 2002). We use the photoelastic  
200 property of gelatin with the purpose of understanding the interaction of the local stresses  
201 with those of the pressurized experimental dike, making a qualitative description of the  
202 changes in the stress field during the intrusion development. The sequence of colored fringes  
203 represents the gradient of the differential stress ( $\sigma_1 - \sigma_3$ ) perpendicular to the light  
204 propagation direction, and the increasing fringe order represents linearly increasing stress  
205 (Crisp, 1952); which in the experiments depend on the caldera diameter and caldera depth.  
206 The photoelasticity experimental setup (Figure 1A) consists of two polarized sheets attached  
207 to the front and back walls of the tank (x-z plane), and two HD video cameras positioned to  
208 record images with polarized light (x-z plane, perpendicular to the dike plane) and artificial  
209 light (y-z plane, parallel to the dike plane).

### 210 **3.2.2. Tracer particle setup**

211 The tracer particle experiment setup requires the use of a high intensity laser that was  
212 configured to fire at 1 Hz and produce a vertical, thin sheet (approximately 1 mm thick) in the  
213 gelatin slab centered on the injection point (Figure 1B, see also Kavanagh et al., 2015). A New  
214 Wave Solo-PIV III Nd-YAG Laser provides 50 mJ pulses of energy between 3 and 5 ns and 532  
215 nm wavelength. The laser firing and acquisition is controlled by Dantec Dynamic Studio  
216 software and synchronized to a MP CCD camera fitted with a 35 mm Nikon lens (Figure 1B).  
217 Longpass (550 nm wavelength) filters fitted to the CCD camera allow only the fluorescent light  
218 reflected by the particles to be captured.

219 A 2D calibration image is required for post-experiment image processing. Prior to the  
220 experiment tank being filled with gelatin, the tank is filled with water and a white calibration  
221 plate with equally-spaced black dots of known size and spacing was aligned with the laser

222 beam in the center of the experimental tank. An image is then captured for later data pre-  
223 processing using DIC.

### 224 **3.3. Data processing**

225 In order to study the evolution of the growing intrusion geometry, we first track the vertical  
226 dike tip trajectory in the x-z plane using video images from the polarized light setup (Figure  
227 1A). This is conducted at intervals of one frame every 5 seconds using the free Java software  
228 Tracker vs 4.10.0 (Brown, 2012). The coordinate origin is set as the top of the needle in the  
229 calibrated model, and the position of the vertical dike tip is manually tracked over time. The  
230 velocity of the dike tip, and the local dip angle relative to horizontal, is simultaneously  
231 computed.

232 DIC is then used to quantify the sub-surface displacement vectors and total strain due to the  
233 dike intrusion, at an interval of one image every 5 seconds (0.2 Hz), by using the commercial  
234 image analysis tool StrainMaster, implemented in the DaVis software package vs. 8 (LaVision).  
235 The calibration image captured prior the experiment is imported into DaVis in a pre-processing  
236 stage to scale the results in dimensional units. This process converts the scale from pixels to  
237 distance units, and corrects any distortions through the de-warping function. The incremental  
238 strain is then calculated by implementing a 'Least Square Matching' algorithm (LSM-  
239 algorithm), which operates using an optical flow approach (Fleet and Weiss, 2006). Three  
240 seeding points are defined within the reference image, and these are static windows of initial  
241 size 121 x 121 pixels that experience no deformation in the experiment. The interrogated area  
242 then increases in size with each iteration implementing the 'region grow' algorithm. Outlier  
243 and Smoothing filters are then applied, and a mask function is added to exclude the tank walls  
244 and caldera cavity from the analysis. The incremental strain is summed to give the total strain.

245 For very small displacement gradients, the strain tensor values are defined by Cauchy's  
246 infinitesimal tensor:

$$247 \quad \epsilon_{ij} = \frac{1}{2} \left( \frac{\partial v_i}{\partial x_j} + \frac{\partial v_j}{\partial x_i} \right) \quad [7]$$

248 where  $v$  is the vector component and  $x$  the spatial axis. As the experiment observations are  
249 carried out in two dimensions ( $x$ - $z$  or  $y$ - $z$  plane), the lineal deformation in the  $x$  or  $y$ -direction  
250 and in the  $z$ -direction are determined by the normal strain components:

$$251 \quad \epsilon_{xx} = \frac{\partial u}{\partial x} \quad \text{or} \quad \epsilon_{yy} = \frac{\partial v}{\partial y} \quad [8]$$

252 and,

$$253 \quad \epsilon_{zz} = \frac{\partial w}{\partial z} \quad [9]$$

254 Thus, the shear strain is given by:

$$255 \quad \epsilon_{xz} = \epsilon_{zx} = \frac{1}{2} \left( \frac{\partial u}{\partial z} + \frac{\partial w}{\partial x} \right) \quad \text{or} \quad \epsilon_{yz} = \epsilon_{zy} = \frac{1}{2} \left( \frac{\partial v}{\partial z} + \frac{\partial w}{\partial y} \right) \quad [10]$$

## 256 **4. Results**

257 In total 19 experiments were conducted to explore the influence of caldera unloading and  
258 injection offset on dike propagation, geometry and growth. The experimental results are  
259 grouped into two end-member geometries: circumferential dikes and cone sheets, however  
260 transition geometries are also observed (see Table 1). We detail our experimental  
261 observations and results below using representative experiments as examples grouped by  
262 their end-member geometries.

### 263 **4.1. Circumferential dikes**

264 Circumferential dikes are formed in our experimental series only in the presence of a small  
265 caldera (Table 1) and in three stages: 1) sub-vertical dike, 2) inclined sheet, and 3) ascent to  
266 eruption (see Supplementary Video Figure S1). When the injection position is offset, these  
267 three stages occur earlier and their transitions happen at greater depth than when the

268 injection is central. The details of each stage of circumferential dike formation and eruption  
269 are now described.

#### 270 **4.1.1. Stage I: Sub-vertical dike**

271 Polarized light shows the unloading stress field induced by the caldera in the pre-injection  
272 state (Figure 2Ai). When the injection starts, a vertical dike is produced (Figure 2Aii and 2Bii)  
273 creating its own stress field that is focused in a small region around the dike tip and  
274 intensifying in magnitude and extent as the dike grows upwards until it reaches a vertical  
275 length of 9.2 cm by the end of this stage (Figure 2Aii). At this time, the dike grows near vertical  
276 with a dip angle of approximately 80° (Figure 3A). During this stage there is an initial rapid  
277 acceleration followed by velocity deceleration (Figure 3B). The DIC analysis (Figure 4) shows  
278 the displacement vectors are small and radiate out from the entire dike length, and the total  
279 normal strain component  $e_{xx}$  (Figure 4Bi) is large ( $14 \times 10^{-2}$ ) compared with the vertical  
280 ( $e_{zz} 4 \times 10^{-2}$ , Figure 4Ci) and shear components ( $e_{xz} 4.5 \times 10^{-2}$ , Figure 4Di).

#### 281 **4.1.2. Stage II: Inclined sheet**

282 In Stage II, the dike moves away from the caldera center with a maximum height of 12.8 cm  
283 in the end of this stage (Figure 2Aiii and 2Biii). In terms of stress, this stage is distinguished by  
284 the colored fringes from the dike visually interacting with those of the caldera (Figure 2Aiii). It  
285 coincides with a rapid decrease in the dip angle (from 80° to 40°, Figure 3A) and a slight  
286 acceleration of the vertical tip (Figure 3B). Overall the direction of displacement is upwards  
287 and towards the caldera, and its maximum amplitude is less than 5 mm (Figure 4Aii, Bii, Cii).  
288 The total strain during Stage II (Figure 4Aii) has slightly decreased in the normal horizontal  
289 strain ( $e_{xx}$  down to  $11 \times 10^{-2}$ ), but has increased in the vertical and shear components  
290 ( $e_{zz}$  and  $e_{xz}$  up to  $10 \times 10^{-2}$  and  $9 \times 10^{-2}$ , respectively);  $e_{xx}$  is distributed along the length

291 of the vertical dike and inclined limb (Figure 4Bii), whereas there are local concentrations in  
292  $e_{zz}$  (Figure 4Cii) and  $e_{xz}$  (Figure 4Dii) at the tip.

### 293 **4.1.3. Stage III: Ascent to eruption**

294 The final stage of circumferential dike development is acceleration to eruption to form a  
295 circumferential fissure (Figure 2Aiv and 2Biv). In our experiments all circumferential dikes  
296 erupted. During this final stage, there is no visual interaction between the dike stress field and  
297 that from the caldera. The dike dip angle gradually increases to 60° and then broadly maintains  
298 this (Figure 3A). The vertical tip decelerates gradually, but then accelerates towards eruption  
299 (Figure 3B). The maximum opening of the inclined limb of the dike is 7.8 mm thick (Figure 4  
300 Aiii), generating the largest magnitude of the total displacement vectors which are oriented  
301 towards the caldera (Figure 4Biii, Ciii, Diii). The total strain just before eruption produces the  
302 maximum deformation during injection, producing visible uplift of the caldera floor. The  
303 largest component of total strain is vertical at  $e_{zz} 22.5 \times 10^{-2}$  (Figure 4Ciii), with similar  
304 values in total horizontal and shear strain ( $e_{xx}$  and  $e_{xz}$  up to  $17.5 \times 10^{-2}$ ; Figure 4Biii and  
305 4Diii).

## 306 **4.2. Cone sheets**

307 Cone sheets were formed in the presence of the large caldera six times (see Table 1), and  
308 transitional geometries (partial cone, but with dike eruption) were formed four times. The  
309 cone sheets are formed in four stages (see Supplementary Video Figure S2), with the first two  
310 stages being identical to the circumferential dike formation. Stage I is a sub-vertical dike, Stage  
311 II is an inclined sheet, Stage III is lateral growth, and Stage IV is cone sheet completion.  
312 Similarly to the circumferential dike, when the injection position is offset this results in earlier  
313 and deeper transitions between the stages.

### 314 **4.2.1. Stage I: Sub-vertical dike, and Stage II: Inclined sheet**



315 The pre-injection stress pattern induced by the large caldera shows more fringes that extend  
316 to greater depths in the gelatin slab (Figure 5Ai) compared to the small caldera (Figure 2Ai).  
317 Similarly to the small caldera experiments, the first two stages of cone sheet growth are: 1)  
318 sub-vertical dike (Figure 5Aii, Bii), which then changes dip and develops into 2) an inclined  
319 sheet (Figure 5Aiii, Biii). During Stage I we observe a moderate decrease in the dip angle from  
320 85° to 75° (Figure 3C) and velocity deceleration (Figure 3D), as the dike reaches 9.3 cm height.  
321 During Stage II the dike changes dip angle from 75° to 35°, accelerates from 0.6 to 1.4 cm/s,  
322 and reaches 12.6 cm height by the end of Stage II.

323 The total displacement and total strain (normal and shear components) of cone sheet growth  
324 are measured in the x-z plane (Figure 6) and y-z plane (Figure 7). During Stages I and II, the  
325 majority of the propagation is out of the y-z plane and so only minor displacements and total  
326 strain are recorded in this view (Figure 7Ai, Bi, Ci, Di, Aii, Bii, Cii, Dii). Stage I of cone sheet  
327 formation (Figure 6Ai) has maximum total strain in the horizontal normal component ( $e_{xx} =$   
328  $11 \times 10^{-2}$ , Figure 6Bi), with this distributed across the whole dike, with lower vertical and  
329 shear total strain components ( $e_{zz}$  and  $e_{xz} = 4 \times 10^{-2}$ ; Figure 6Ci and 6Di). In contrast, Stage  
330 II has maximum total strain in the vertical normal component ( $e_{zz} = 12 \times 10^{-2}$ ; Figure 6Cii),  
331 with lower horizontal and shear total strain components ( $e_{xx}$  and  $e_{xz} = 8 \times 10^{-2}$ ; Figure 6Bii  
332 and 6Dii). There are also similar displacement vectors to those observed in Stages I and II of  
333 the circumferential dike formation, with low magnitude displacements (<5 mm in Stage I, and  
334 5-10 mm in Stage II) radiating out from the dike.

#### 335 **4.2.2. Stage III: Lateral dike growth by arcuate segments**

336 Following initial vertical dike growth (Stage I) and then divergence to a dipping dike (Stage II),  
337 a new direction of intrusions establishes at the turning point  $h$  (see Table 1). Stage III of cone  
338 sheet growth is marked by the Stage II dike dip angle stabilizing at approximately 60° (Figure

339 3C), and the vertical growth rapidly decelerating indicating an arrested dike (Figure 3D). Two  
340 circumferential and laterally-propagating en echelon arcuate segments then form close to the  
341 turning point (Figure 3C), specifically from the lower part of the inclined sheet (Figure 5Aiv  
342 and 5Biv). In the x-z plane, the total displacement vectors increase in magnitude relative to  
343 Stage II to be >10 mm, and the maximum displacement continues being oriented radially  
344 towards the caldera (Figure 6Biii, Ciii, Diii). The largest total strain is the vertical normal  
345 component ( $e_{zz} = 37.5 \times 10^{-2}$ ; Figure 6Ciii) followed by the shear component ( $e_{xz} = 23 \times$   
346  $10^{-2}$ ; Figure 6Diii) and horizontal normal component ( $e_{xx} = 20 \times 10^{-2}$ ; Figure 6Biii). In Stage  
347 III, the cone sheet emerges in the y-z plane as the inclined, laterally-propagating arcuate  
348 segments penetrate the laser sheet (Figure 7Aiii). This produces maximum total displacement  
349 of 10 mm (which is slightly less than measured in the x-z plane), and a maximum vertical  
350 deformation ( $e_{zz} = 12 \times 10^{-2}$ ; Figure 7Ciii) compared to horizontal ( $e_{yy} = 7 \times 10^{-2}$ ; Figure  
351 7Biii) and shear components ( $e_{yz} = 9 \times 10^{-2}$ ; Figure 7Diii); which are all lower than strains  
352 measured in the x-z plane.

#### 353 **4.2.3. Stage IV: Cone sheet completion**

354 The fourth and final stage of cone sheet formation is the completion of the cone geometry  
355 (Figure 5Av and 5Bv). This occurs when the laterally-propagating arcuate segments of Stage III  
356 join to create a circular profile in the horizontal plane without erupting. The final cone sheet  
357 geometry has a range of forms spanning 'cocktail-glass', 'bowl' and 'trumpet' forms (Figures  
358 5, 6 and 7), in agreement with cone sheet geometries described by Burchardt et al. (2018). In  
359 transitional geometries, Stage III still produces the lateral sub-surface arcuate segments but  
360 they do not join. Instead, at some moment the vertical ascent of the dike is reinitiated, at the  
361 location where it first became arrested, and this results in an eruption. Therefore, transitional

362 geometries do not reach Stage IV and have growth behavior and a final geometry that is  
363 intermediate to the circumferential dike and cone sheet.  
364 Stage IV has a slight decrease in the dip angle starting immediately after the arcuate segments  
365 join (Figure 3C), and the velocity decrease is maintained (Figure 3D). The thickest opening of  
366 the inclined sheet was 13.63 mm (Figure 6Aiv), which produced displacements greater than  
367 10 mm focused directly beneath and towards the caldera (Figure 6Biv, Civ, Div). The maximum  
368 strain occurs in the vertical normal component, reaching  $e_{zz} = 55 \times 10^{-2}$  in the x-z plane  
369 (Figure 6Civ) and  $e_{zz} = 50 \times 10^{-2}$  the y-z plane (Figure 7Civ). The total strain is up to  $e_{xx} =$   
370  $20 \times 10^{-2}$  and  $e_{yy} = 12 \times 10^{-2}$  in the horizontal components (Figures 6Biv and 7Biv,  
371 respectively), and  $e_{xz} = 35 \times 10^{-2}$  and  $e_{yz} = 22.5 \times 10^{-2}$  in the shear component (Figures  
372 6Div and 7Div, respectively).

## 373 5. Discussion

### 374 5.1. Circumferential dike or cone sheet? Comparison with previous experiments

375 Our experimental series has produced a spectrum of thin sheet-like intrusions, all of which  
376 were parallel to the circular caldera, and with end-member geometries of an erupted  
377 circumferential dike (Figure 2) and an intrusive cone sheet (Figure 5). The development of  
378 these different end-member geometries was similar. Both circumferential dikes and cone  
379 sheets propagated at dip angles which reached almost vertical (Figure 3A, C; Figure 8), but the  
380 circumferential dikes dip angle ranged from  $\sim 40^\circ$  compared to  $30^\circ$  for the cone sheets (Figure  
381 8). These dip values are similar to those in nature, for example the trachytic to phonolitic cone  
382 sheets of the Tejada Complex, Gran Canaria which intruded intra-caldera deposits (Schirnick  
383 et al., 1999), and the mafic cone sheets of the Ardnamurchan central igneous complex, NW  
384 Scotland which intruded into the base of an ancient basaltic volcano (Richey and Thomas,  
385 1930).

386 Circumferential dikes and cone sheet geometries have been studied in previous laboratory  
387 experiments. Using a granular material to represent the properties of the brittle crust and a  
388 flat topography, Galland et al. (2014) found that cone sheets form when the magma source is  
389 shallow with respect to the intrusion's width, or when the injection velocity or viscosity is high.  
390 Corbi et al. (2016) created buoyant air-filled dikes in gelatin edifices which had a topographic  
391 depression simulating a caldera. Similarly to our experiments, they observed that the  
392 unloading stress field leads to the formation of circumferential dikes. They found that magma  
393 buoyancy plays a key role in the dike geometry and the eruption location, and our experiments  
394 support this work even though we did not include a volcanic edifice. When the unloading  
395 stresses were particularly large we found this was able to stop eruption and cause a full-cone  
396 sheet to develop, whereas Corbi et al. (2016) did not form cone sheets.

397 The caldera diameter was the key parameter in determining the outcome of our experiments:  
398 circumferential dikes always developed in the presence of the 9 cm caldera diameter, and a  
399 spectrum of transitional to cone sheet geometries were associated with the 12 cm caldera  
400 diameter topography (see Table 1). Following the approach of Galland et al. (2014), we have  
401 analyzed our experiments further by considering the outcomes related to dimensionless Pi-  
402 numbers (Figure 9). The first Pi-number is geometric:

$$403 \quad \Pi_1 = \frac{h}{d} \quad [11]$$

404 where  $h$  is the depth at which bending of the dike first occurs, and  $d$  is the horizontal extent  
405 of the intrusion (see Table 1). The second Pi-number considers the fluid-flow properties and  
406 extent of unloading stress relative to lithostatic loading:

$$407 \quad \Pi_2 = \frac{\mu v}{d(P_L - P_U)} \quad [12]$$

408 where  $\mu$  is the fluid viscosity,  $V$  is the velocity of the fluid,  $P_L$  is the lithostatic pressure, and  $P_U$   
409 is the unloading pressure due to the presence of the caldera (see Supplementary Table S1).  
410 Figure 9 shows our experiments occupy three distinct regions in this non-dimensional space,  
411 with cone sheets forming at low  $\Pi_1$  and  $\Pi_2$  values, circumferential dikes forming at high  $\Pi_1$   
412 and  $\Pi_2$  values, and transitional geometries forming at intermediate  $\Pi_1$  and  $\Pi_2$  values.  
413 Geophysical constraints on parameter values that would populate the  $\Pi_1$  and  $\Pi_2$  equations in  
414 nature (see Supplementary Table S1 for example) suggest that magnitudes of  $\Pi_1$  and  $\Pi_2$  in  
415 nature are high compared to our experiments. For example, at Rabaul Volcano in Papua New  
416 Guinea (Kennedy et al., 2018) the corresponding  $\Pi_1$  value is 1.5 and the  $\Pi_2$  value is  $3 \times 10^{-5}$ .  
417 This means, according to our models, the most likely intrusion form geometry at Rabaul  
418 Volcano would be circumferential dikes.

## 419 **5.2. Circumferential dikes and cone sheets in nature**

420 The Ardnamurchan cone sheets are perhaps the most-famous of all cone sheets, but there are  
421 contrasting models to explain their origin. Burchardt et al. (2013) used 3D projections to  
422 propose that the Ardnamurchan cone sheets originate from a single, elongated and  
423 temporally evolving magma chamber. This model is in contrast to Richey and Thomas (1930)  
424 who originally proposed three centers, and Magee et al. (2012) who proposed lateral magma  
425 flow from an adjacent magmatic source in a compressional stress field. We show  
426 experimentally that local unloading stresses can cause an initially vertical dike originating from  
427 directly beneath a caldera to stall in the crust and grow laterally to form a cone sheet. This is  
428 relevant to the Ardnamurchan central igneous complex, as our model does not require input  
429 from neighboring systems to build a cone sheet (in contrast to Magee et al., 2012) and does  
430 not make assumptions about the nature of the magma chamber at depth (as is the case in  
431 Burchardt et al., 2013). Instead we demonstrate that such geometries could be formed purely

432 due to local unloading stresses. It is unclear whether or not there was a caldera present at the  
433 time when the Ardnamurchan cone sheets formed (Brown and Bell, 2006), but calderas are  
434 thought to have been present in the region at the time of intrusion (Troll et al., 2000).

435 Articulated magma intrusion geometries, made up of circumferential sub-vertical dikes close  
436 to the caldera rim which dip towards sub-horizontal sills below the caldera floor, have often  
437 been needed to fit crustal deformation data at calderas. Geodetic studies of magma intrusion  
438 associated with the 2005 circumferential fissure eruption of Fernandina volcano in the  
439 Galapagos (summit caldera: 5 km x 6.5 km) presented pre-eruptive (Bagnardi et al., 2013) and  
440 co-eruptive (Chadwick et al., 2011) surface deformation that was recorded using  
441 Interferometric synthetic aperture radar (InSAR). Inverse models of the data suggested the  
442 intrusion which fed the eruption had a curved and circumferential laminar geometry and  
443 originated from a sill, thus showing similar geometry to our experimental circumferential  
444 dikes. The continuous vertical growth and final eruption of our experimental circumferential  
445 dike agrees well with the Chadwick et al. (2011) model of intrusion leading to the 2005  
446 eruption of Fernandina (Corbi et al., 2015).

447 Overall, we suggest that the common modeling assumption of flat geometries, such as planar  
448 sheets opening dislocations or cracks, the availability of suitable analytical solutions, and the  
449 need to keep the number of model parameters low, may have limited our ability to recognize  
450 curved geometries such as those we propose here. Deep cone sheet intrusions may produce  
451 low-amplitude uplift that may be a satisfyingly fit for pressurized sub-horizontal cracks below  
452 the caldera floor, which is a feature ubiquitously found by geophysical and geodetic surveys  
453 at calderas worldwide.

### 454 **5.3. Arcuate segment development and lateral dike growth**

455 Lateral propagation of a circumferential dike has been evidenced by geological records, but  
456 rarely from geophysical monitoring. Geological evidence of lateral flow during cone sheet  
457 development was found by Magee et al. (2012) using magnetic fabrics preserved within  
458 crystalline cone sheets. However, they interpreted this as evidence of magma being sourced  
459 from an adjacent magma chamber, but our results show that such crystalline fabrics could  
460 result from a cone sheet intrusion whose magma source was directly beneath an unloaded  
461 topography. Geophysical evidence of lateral propagation of a circumferential dike firstly came  
462 from the 1989 seismic swarm at Mammoth Mountain, Long Valley caldera, California (Prejean  
463 et al., 2003) where earthquake hypocenter migration into a ring structure was interpreted as  
464 fluid which triggered seismicity on a ring fault, but it would be also consistent with lateral  
465 propagation (0.4 km/month) of a conical opening crack filled with magma or other magmatic  
466 fluid evidenced by the migration of seismicity over time. Therefore, our model observations  
467 are support the interpretation of lateral magma migration recorded by the seismic data.  
468 Secondly, reconstructing ground displacement at the pre-eruptive phase in Monte Nuovo,  
469 Campi Flegrei caldera (1935 AD), Di Vito et al. (2016) recognized a circumferential source  
470 extending from the center, eccentrically towards the caldera rim, that transfers felsic magma  
471 laterally to feed eruptions at the caldera margin, which has been the eruptive magma path for  
472 the last 5 ka. In the laboratory, both circumferential dikes and cone sheets had their lowest  
473 ascent velocities when the dikes were growing at intermediate dip angle (40-80°), and their  
474 highest velocities coincided with the lowest and highest dip angles (Figure 8).

475 Circumferential lateral propagation was present in the growth of our experimental cone sheet  
476 intrusions by the establishment of laterally propagating arcuate segments, and the cone sheet  
477 geometry initiated at the bending location of the dike ( $h$ ). We interpret the development of  
478 en echelon arcuate segments in our experiments to be associated with stress rotation, due to

479 the influence of the caldera stress field which causes lateral propagation and crack opening  
480 under mixed-mode loading (Mode I and Mode III) thus creating shear at the growing tip  
481 (Pollard et al., 1982).

#### 482 **5.4. Limitations of our models**

483 Our experimental approach was not to reproduce the natural complexity of magma intrusion  
484 in the presence of calderas, but to focus on the effect of the magnitude and extent of the  
485 unloading stress on the type of intrusion formed and how it grew. Inelastic host-rock  
486 deformation was not considered in our models, and yet this may be important in the shallow  
487 crust and in a caldera setting in particular, where rocks may have been damaged due to the  
488 caldera-forming process (see Galland et al., 2018 for a review). On a local scale, an inelastic  
489 host-rock rheology may dampen the transference of rock deformation signals, due to local  
490 compaction and grain rotation, and may increase the possibility of dike segmentation  
491 occurring. We did not consider rock layering, yet volcanic settings are likely to be mechanically  
492 variable, and previous work has demonstrated how rigidity layering can promote the  
493 formation of sills beneath a rigid layer (Kavanagh et al., 2006). Calderas also have fault systems  
494 that are likely to influence magma propagation (Browning and Gudmundsson, 2015). Recent  
495 experimental work using particle image velocimetry (Kavanagh et al., 2018; Kavanagh, 2018)  
496 to model magma flow in dikes is challenging existing dike propagation models, and  
497 demonstrates how consideration of the host rock deformation and the magma flow dynamics  
498 are needed to develop the next generation of dike emplacement models. The additional  
499 impacts of faults, mechanical layering and magma flow dynamics on magma propagation in  
500 caldera settings should be the focus of future multidisciplinary and experimental work.

#### 501 **6. Conclusions**



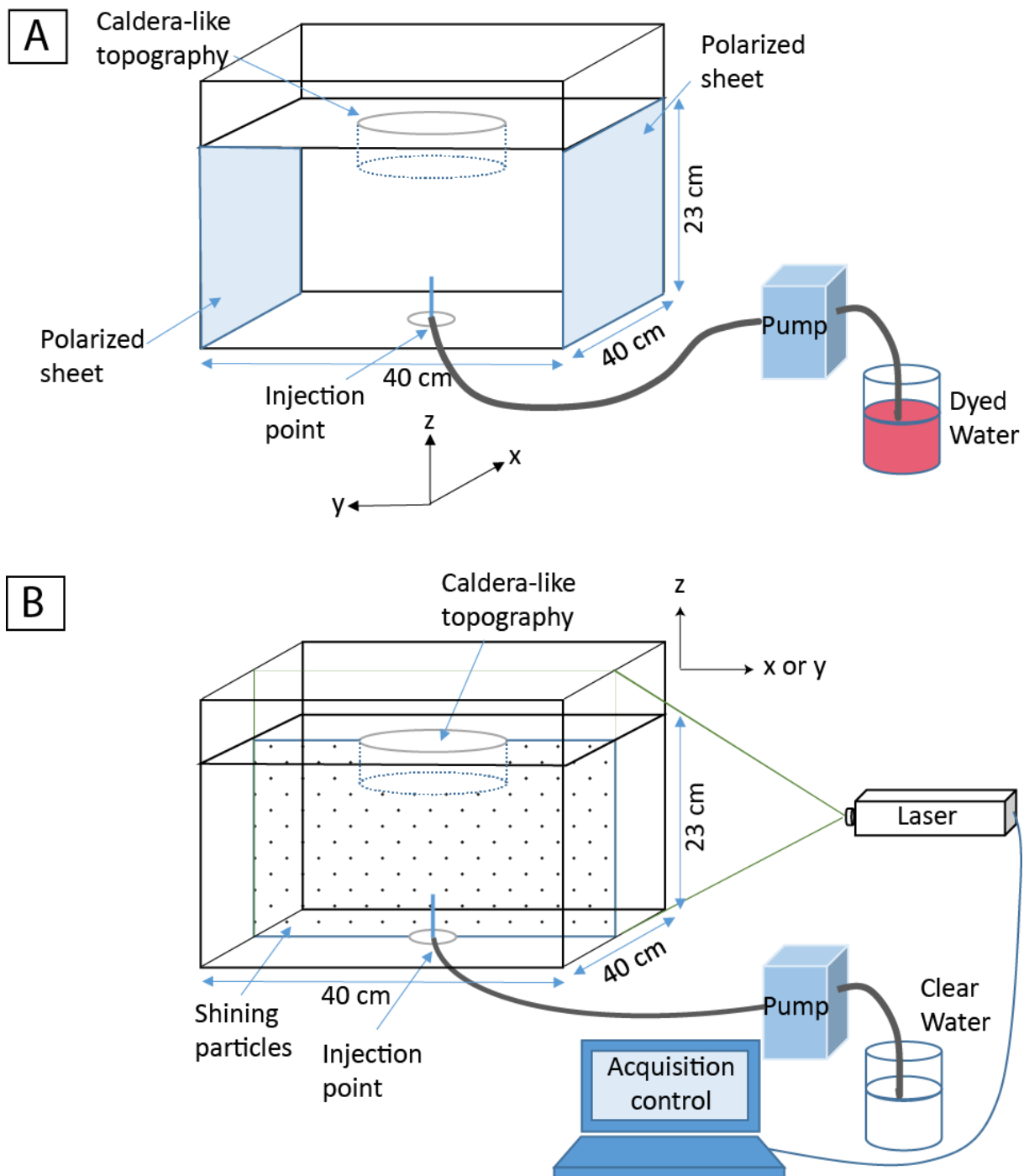
502 We produced experimental circumferential dikes which erupted, and intrusive cone sheets  
503 that grew by lateral propagation of en echelon arcuate dike segments. Both originated from a  
504 single dike beneath a caldera-like topography in an elastic material. We also formed  
505 transitional geometries that were intermediate to these end-member forms. Circumferential  
506 dike and cone sheet intrusion dynamics occurred in stages of development which are reflected  
507 by their geometric (dip angle), kinematic (velocity) and dynamic (stress and strain) evolution.  
508 We identified 3 stages of circumferential dike development (I. Sub-vertical dike; II. Inclined  
509 sheet; III. Ascent to erupt) and 4 stages of cone sheets (I. Sub-vertical dike; II. Inclined sheet;  
510 III. Lateral growth by arcuate en echelon dike segments, and IV. Completion of the cone sheet).  
511 Our results show there are many similarities between the dynamics of cone sheets and  
512 circumferential dikes. Our summative dimensionless phase diagram suggests that their  
513 occurrence can be related to geometric, fluid flow, and lithospheric unloading conditions.  
514 We have proposed a new origin and emplacement for cone sheets that originate from purely  
515 vertical dike growth. However, our analysis suggests that conditions in nature seem to be  
516 unfavorable for cone sheets to form due to crustal unloading in a caldera setting, and that  
517 circumferential dikes and transitional-cone sheet geometries are more likely to form. Our  
518 models can help the interpretation of InSAR, GPS and seismic data from active systems, and  
519 contribute to the production of more accurate models of magma sources beneath calderas.  
520 An important new implication of our models for volcano monitoring is that the conditions for  
521 circumferential dike formation appear to be more prevalent in nature. Significantly, it may not  
522 be possible to distinguish whether an intrusion will be likely to erupt or not until it has  
523 propagated into the shallow crust, which is when it is also likely to be propagating at its fastest  
524 rate. This new understanding of magma intrusion dynamics will help to reconstruct the history  
525 of ancient calderas, and to forecast unrest and eruptions in active ones.

526 **Acknowledgments**

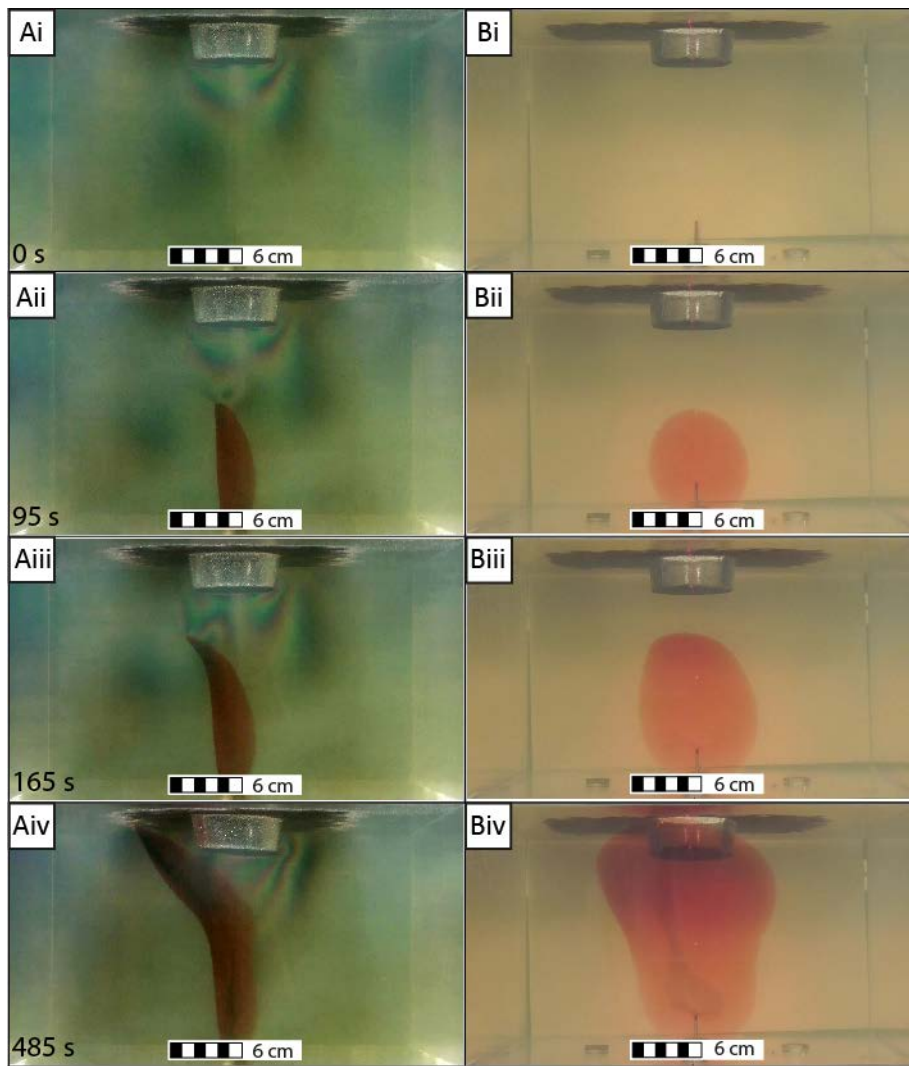
527 This research was supported by the German Research Centre for Geosciences, GFZ and the  
528 ERC Volcapse project, and by the program Forschungsstipendium für Doktorat from Deutscher  
529 Akademischer Austausch Dienst DAAD awarded to AG. AG and SHH wish particular thanks to  
530 members of the Liverpool MAGMA Laboratory Elliot Wood and Simon Martin for their  
531 assistance in the development of this work. SHH acknowledges support from the Malaysian  
532 Government and the National University of Malaysia. AG especially thanks to Mehdi Nikkhoo  
533 for long discussions and advice related to this work and other topics and for help with  
534 conducting earlier models. We thank Steffi Burchardt and Craig Magee for thoughtful reviews  
535 which improved the manuscript, and we thank Tamsin Mather for editorial support.

Experiment code	C [cm]	X [cm]	D [cm]	Wt.%	H [cm]	t [hr]	T [°C]	E [Pa]	Q [m <sup>3</sup> /s]	Result	h [cm]	d [cm]	Analysis Method
AG-07	9.0	0.0	3.31	2.5	22.6	20.5	5	2675	$3.9 \times 10^{-7}$	C. dike	8.2	13.0	PL, TT
AG-13	9.0	0.0	3.78	2.5	23.1	20.5	5	2843	$3.9 \times 10^{-7}$	C. dike	10.7	13.3	TP
AG-09	9.0	1.0	3.04	2.5	23.2	21.0	5	2490	$3.9 \times 10^{-7}$	C. dike	8.8	13.8	PL, TT
AG-08	12.0	0.0	3.94	2.5	23.5	20.0	5	3113	$3.9 \times 10^{-7}$	Cone sheet	12.1	22.4	PL, TT
AG-06	12.0	0.0	3.52	2.5	22.4	19.8	5	2779	$3.9 \times 10^{-7}$	Cone-Trans	10.7	17.5	-
AG-14	12.0	0.0	4.20	2.5	23.5	21.0	5	2739	$3.9 \times 10^{-7}$	Cone-Trans	11.1	16.9	-
AG-15	12.0	0.0	3.65	2.5	23.5	21.1	5	2586	$3.9 \times 10^{-7}$	Cone-Trans	9.8	17.7	-
AG-16	12.0	0.0	3.77	2.5	23.2	20.5	5	2902	$3.9 \times 10^{-7}$	Cone-Trans	16.8	17.5	-
AG-10	12.0	1.0	3.55	2.5	22.5	21.0	5	2401	$3.9 \times 10^{-7}$	Cone sheet	12.0	23.4	PL, TT
AG-05	12.0	1.0	3.58	2.5	23.1	19.7	5	2721	$3.9 \times 10^{-7}$	Cone sheet	14.3	23.7	TT
AG-17	12.0	1.0	3.95	2.5	23.2	19.7	5	2580	$3.9 \times 10^{-7}$	Cone sheet	15.2	24.5	TP
AG-19	12.0	1.0	3.80	2.5	23.1	19.0	5	2964	$3.9 \times 10^{-7}$	Cone sheet	15.3	24.0	TP
AG-18	12.0	2.0	3.90	2.5	23.2	22.0	5	3031	$3.9 \times 10^{-7}$	Cone sheet	14.5	23.9	TP

537 **Table 1:** Model parameters, observed results, and methods applied in the experiment analysis. The experiments are listed in order of caldera  
538 diameter C and offset injection position X. The measured caldera depth D, gelatin concentration Wt.%, thickness of gelatin slab H, time left to cure  
539 t, refrigerator temperature T, average Young's modulus E, and injection flux of fluid Q is reported. 'Result' corresponds to the final geometry of the  
540 intrusion classified as 'C. dike' (circumferential dike), 'Cone sheet', or 'Cone-Trans' for transitional geometries, and the final depth of bending h, and  
541 extent of intrusion d are also reported. The analysis methods used are: Polarized light (PL), vertical tip tracking (TT) and tracer particles (TP).

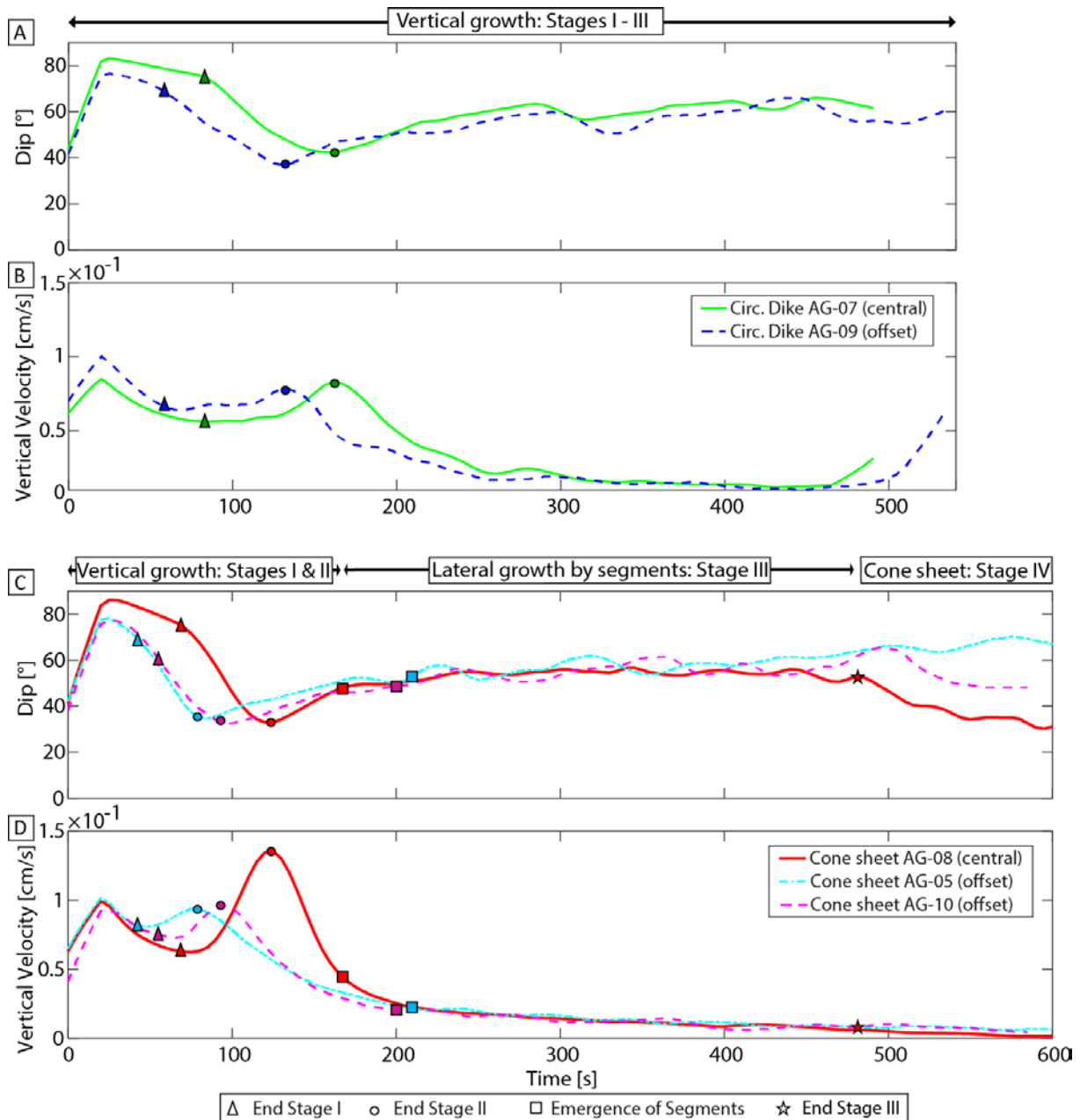


542  
 543 **Figure 1:** Schematic diagram of the experimental setups. A) Polarized light experiment: dyed  
 544 water is injected into the base of a gelatin slab using a peristaltic pump. The gelatin surface is  
 545 modeled to have a caldera-like topography, and stress in the gelatin is visualized using two  
 546 parallel polarized sheets attached to the tank walls on the x-z plane and perpendicular to the  
 547 initial dike profile. Two HD video cameras (not shown) record images the x-z and y-z directions.  
 548 B) Tracer particle experiment: a high intensity vertical laser sheet illuminates a 2D profile  
 549 (either x-z plane or y-z plane) through the center of the tank and exciting passive-tracer  
 550 fluorescent particles in the gelatin. A CCD camera records the illuminated plane at 1 frame per  
 551 second, synchronized with the laser.

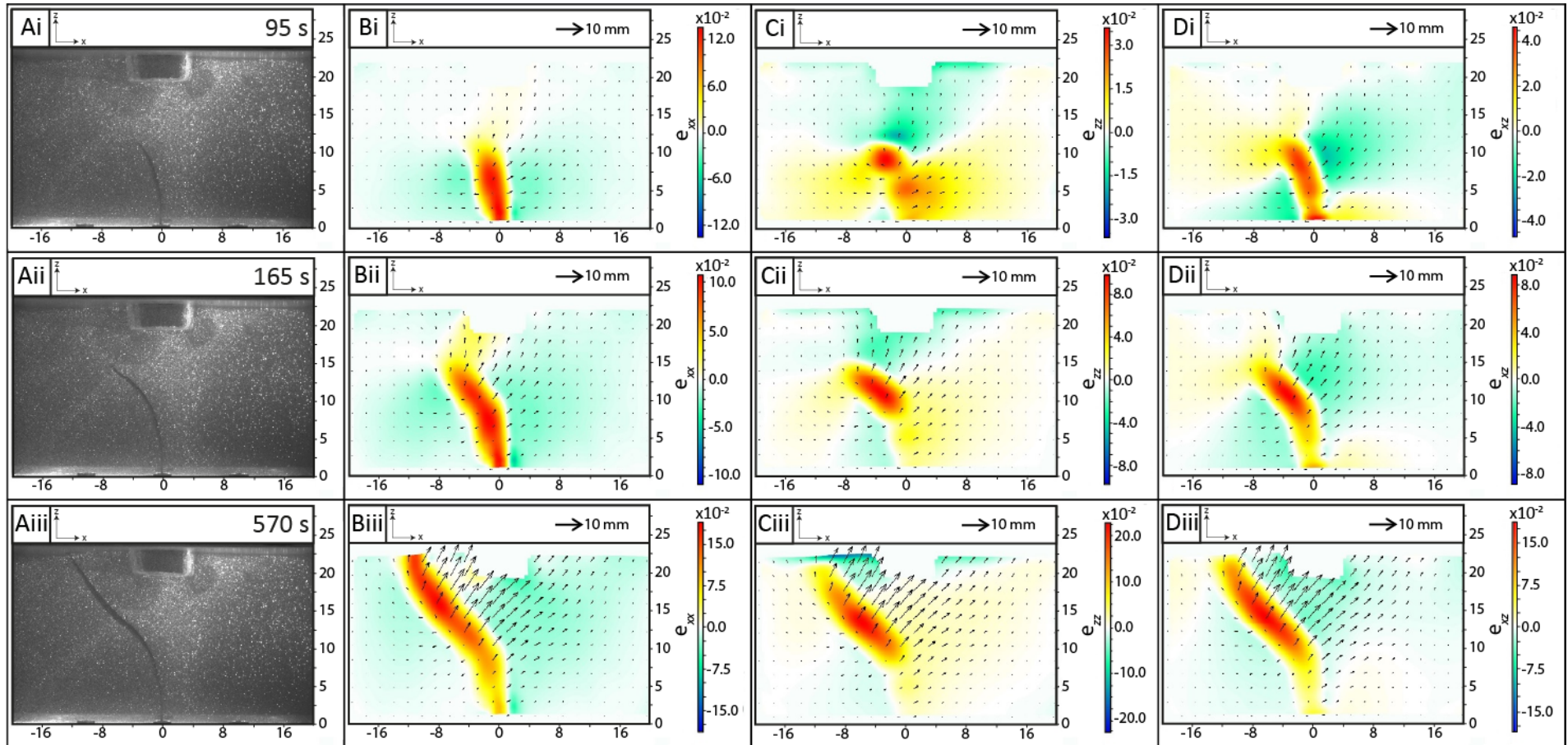


552

553 **Figure 2:** Photographs of circumferential dike development in the presence of a small caldera  
 554 (Experiment AG-07, see Table 1): A) Polarized light (x-z plane), and B) artificial light (y-z plane).  
 555 i) Pre-injection state, ii) Stage I: sub-vertical dike (95 s), iii) Stage II: inclined sheet (165 s), iv)  
 556 Stage III: ascent to eruption (485 s). See also Supplementary Video Figure S1.



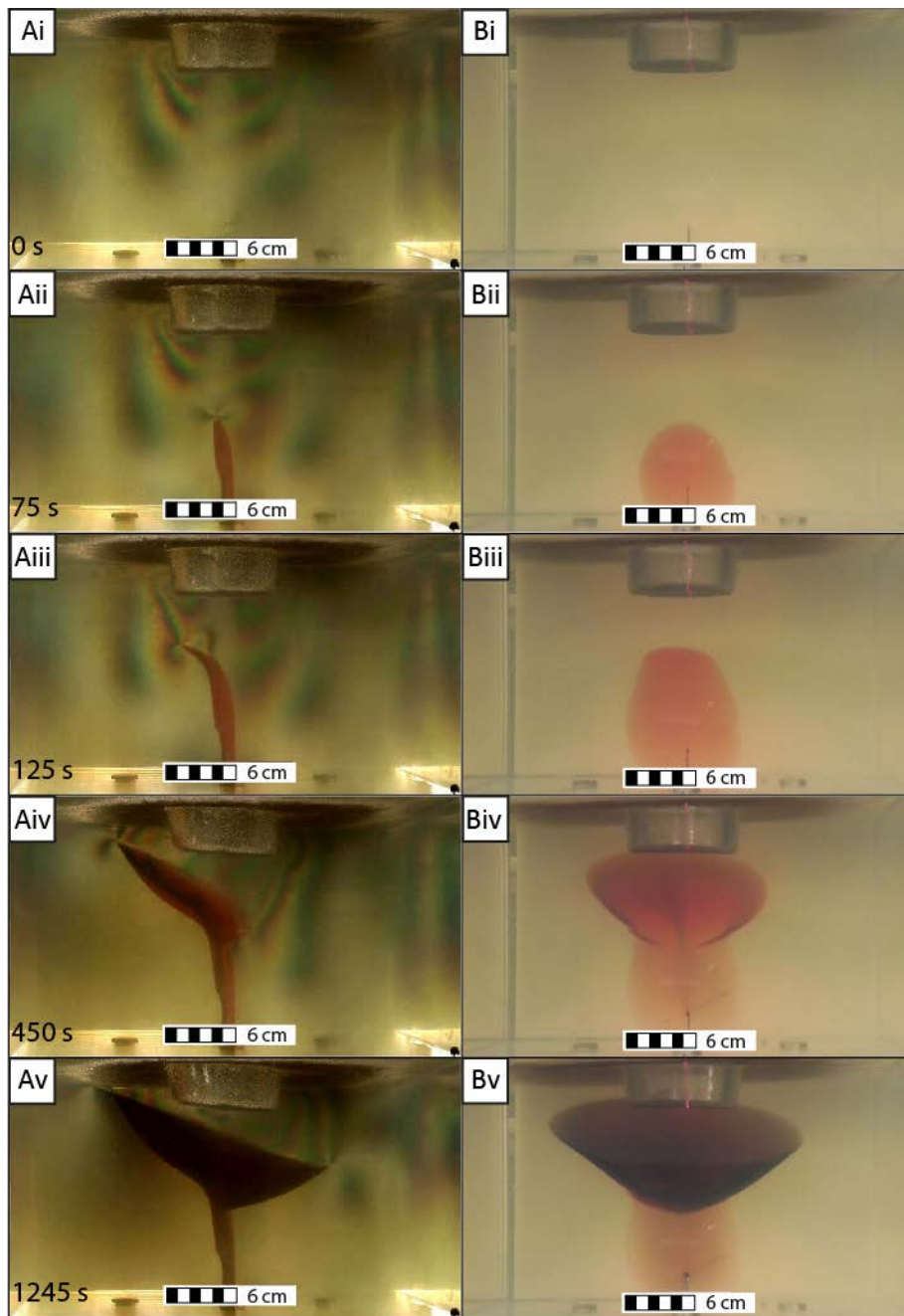
557  
 558 **Figure 3:** Three stages of circumferential dike (A-B) and four stages of cone sheet (C-D) growth  
 559 shown by changes in Dip angle (°) and velocity (cm/s) of the vertical dike tip in the presence  
 560 of the caldera. The approximate timings of stage transitions is indicated at the top of the  
 561 graphs (A for circumferential dikes, and C for cone sheets). In the graphs the triangle indicates  
 562 the end of Stage I (sub-vertical dike), the circle indicates the end of Stage II (inclined sheet),  
 563 and the star indicates the end of Stage III (lateral growth by arcuate segments in cone sheet  
 564 emplacement). Stage III shows the ascent to eruption in circumferential dike emplacement.  
 565 The Stage III of cone sheet growth produces laterally propagating arcuate segments (the time  
 566 of their emergence is indicated by a square) and these join at the start of Stage IV to complete  
 567 the geometry.



568

569 **Figure 4:** Three stages of circumferential dike development in the presence of a small caldera, imaged in the x-z plane, with sub-surface total strain  
 570 (color maps) and displacement (vector arrows) calculated using DIC (Experiment AG-13, see Table 1): i) Stage I: initial sub-vertical dike (95 s), ii)  
 571 Stage II: inclined sheet (165 s), and iii) Stage III: ascent to eruption (570 s). A) Dewarped experimental images, B) horizontal total normal strain  $e_{xx}$ ,  
 572 C) vertical total normal strain  $e_{zz}$ , and D) total shear strain component  $e_{xz}$  are shown. The red color represents extensional deformation in the  
 573 normal components and anticlockwise rotational deformation in the shear component. See also Supplementary Video Figure S1.

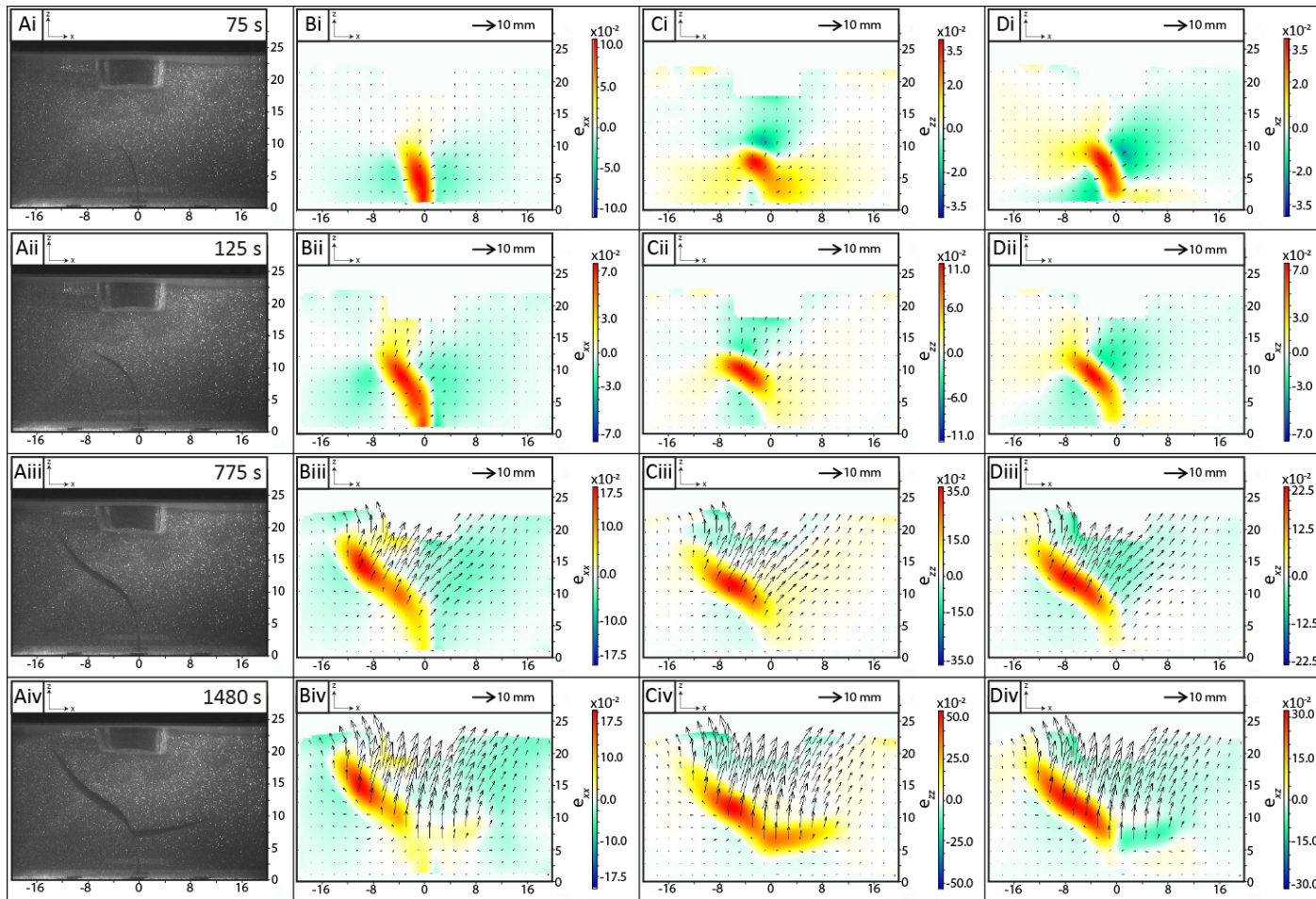




574

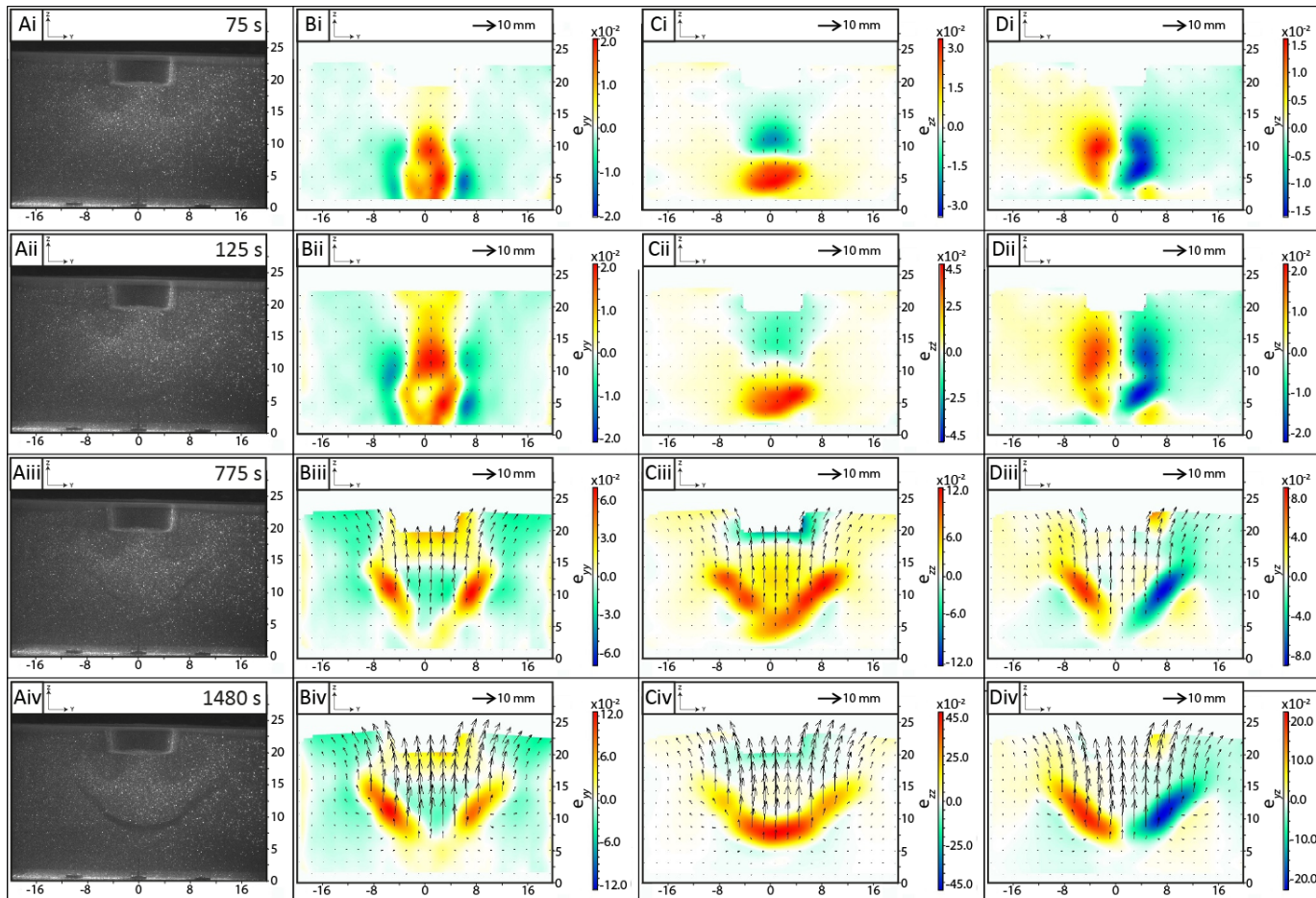
575 **Figure 5:** Photographs of cone sheet development in the presence of a large caldera  
 576 (Experiment AG-08, see Table 1): A) Polarized light (x-z plane), B) artificial light (y-z plane). i)  
 577 Pre-injection stress state, ii) Stage I: sub-vertical dike (75 s), iii) Stage II: inclined sheet (125 s),  
 578 iv) Stage III: lateral growth by en echelon arcuate segments (450 s), and v) Stage IV: cone sheet  
 579 completion with no eruption (1245 s). See also Supplementary Video Figure S2.





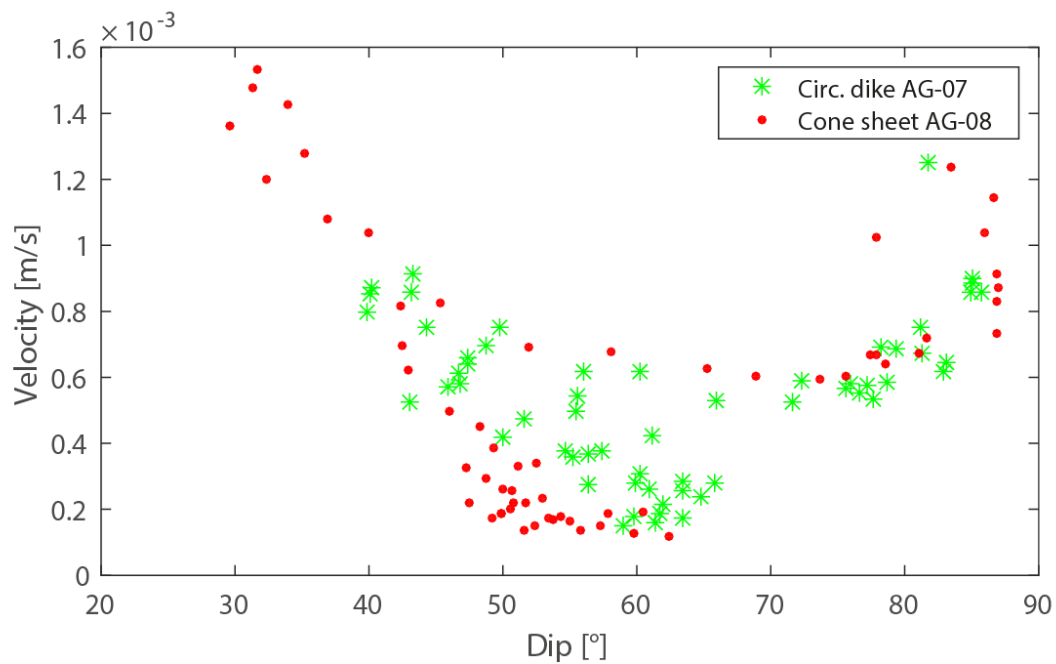
580

581 **Figure 6:** Cone sheet development in the presence of a large caldera, viewed in the  $x$ - $z$  plane, with sub-surface total strain (color maps) and  
 582 displacement (vector arrows) calculated using DIC (Experiment AG-17, see Table 1). Four stages of cone sheet development are shown: i) Stage I:  
 583 initial sub-vertical dike (75 s), ii) Stage II: inclined sheet (125 s), iii) Stage III: arrest and increased opening of the inclined sheet (775 s), and iv) Stage  
 584 IV: cone sheet geometry completion with no eruption (1480 s). A) Dewarped experimental images, B) horizontal total normal strain  $e_{xx}$ , C) vertical  
 585 normal strain  $e_{zz}$ , and D) shear strain component  $e_{xz}$ . The red color represents extensional deformation in the normal components and anticlockwise  
 586 rotational deformation in the shear component. See also Supplementary Video Figure S3.

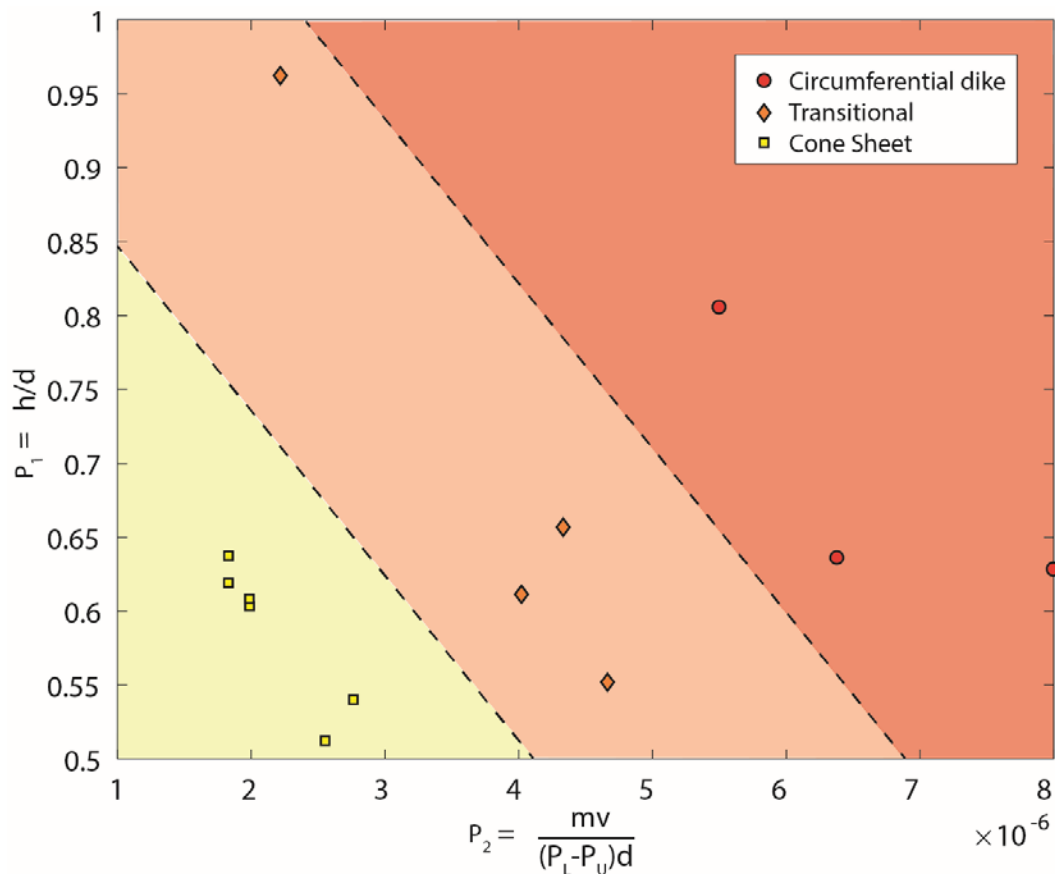


587

588 **Figure 7:** Cone sheet development in the presence of a large caldera, viewed in the  $y$ - $z$  plane, with sub-surface total strain (color maps) and  
 589 displacement (vector arrows) calculated using DIC (Experiment AG-19, see Table 1). Four stages of cone sheet development are shown: i) Stage I:  
 590 initial sub-vertical dike (75 s), ii) Stage II: inclined sheet (125 s), iii) Stage III: arrest and increased opening of the inclined sheet (775 s), and iv) Stage  
 591 IV: cone sheet geometry completion with no eruption (1480 s). A) Dewarped experimental images, B) horizontal normal strain  $e_{yy}$ , C) vertical normal  
 592 strain  $e_{zz}$ , and D) shear strain component  $e_{yz}$ . The red color represents extensional deformation in the normal components and anticlockwise  
 593 rotational deformation in the shear component. See also Supplementary Video Figure S4.



594  
 595 **Figure 8:** The local dip angle relative to vertical ascent velocity for circumferential dike (AG-  
 596 07) and cone sheet development (AG-08). See Table 1 for experimental conditions.



597  
 598 **Figure 9:** Dimensionless phase diagram presenting the range of intrusion geometries formed  
 599 in the experiments: circumferential dikes (red circles), Transitional geometries (orange  
 600 diamonds) and cone sheets (yellow squares). The dimensionless parameters represent the  
 601 model conditions  $\Pi_1 = h/d$  and  $\Pi_2 = \mu v / (P_L - P_U)d$ . The cone sheets and circumferential  
 602 dikes plot in distinct fields with transitional geometries formed in the intermediate zone.

	Parameter (units) or Equation	Nature (range)	Nature (preferred value)	Experiments (range)	Experiments (preferred value)	Scaling ratio	
<b>Medium and fluid properties</b>							
	Host medium density <sup>1</sup>	$\rho_r$ (kg m <sup>-3</sup> )	2300 - 3000	2700	994 – 1002	1002	0.37
	Fluid density <sup>2</sup>	$\rho_f$ (kg m <sup>-3</sup> )	2000 - 2800	2680	990 – 996	996	0.37
	Fluid viscosity <sup>10</sup>	$\mu$ (Pa s)	0.1 – 1E+23	100	8.9E-4	8.9E-4	8.9E-6
	Density difference <sup>3</sup>	$\Delta\rho = \rho_r - \rho_f$	1 - 300	20	4 - 6	6	0.3
	Poisson's ratio <sup>4</sup>	$\nu$	0.1 – 0.35	0.25	0.495-0.5	0.499	2
	Fracture toughness <sup>5</sup>	$K_c$ (Pa m <sup>1/2</sup> )	3E+8 – 1E+9	1E+9	24 - 80	80	8E-8
	Acceleration due to gravity	$g$ (m s <sup>-2</sup> )	-	10	-	10	1
<b>Geometry</b>							
	Geometric length	$L$ (m)	-	1E+3	-	0.01	1E-5
	Caldera diameter	$C$ (m)	9E+3 – 12E+3	12E+3	0.09 – 0.12	0.12	1E-5
	Caldera depth	$D$ (m)	3E+3 – 4.5E+3	4E+3	0.03 – 0.045	0.04	1E-5
	Depth of intrusion <sup>11</sup>	$h$ (m)	3E+3 – 17E+3	13.5E+3	0.08 – 0.16	0.15	1.1E-5
<b>Scaling expressions</b>							
<b>Lengths</b>							
	Buoyancy length <sup>6</sup>	$L_b = (K_c / (\pi^{1/2} \Delta\rho g))^{2/3}$	3.2E+3 – 6.6E+4	19965	0.83 – 1.22	0.83	4.1E-5
<b>Stresses</b>							
	Elastic deformation <sup>7</sup>	$\sigma = Ee$	1E+6 - 4E+7	2E+7	4.5 - 75	60	3E-6
	Lithostatic load	$P_L = \rho_r g h$	6.7E+7 – 5E+8	3.6E+8	779 - 1571	1473	4.1E-6
	Unloading <sup>8</sup>	$P_U = \rho_r g D$	6.9E+7 – 1.3E+8	1.1E+8	298 – 451	401	3.7E-6
	Young's Modulus <sup>9</sup>	$E$	1E+9 - 1E+10	1E+10	300 - 3000	3000	3E-7
<b>Strain</b>							
	Thickness/width	$e$	1E-3 - 4E-3	2E-3	1.5E-2 - 2.5E-2	2E-2	10

603 **Supplementary Table S1:** Parameters and equations implemented to scale the experiments, including their ranges and the preferred values we  
604 have selected in nature and the experiments (<sup>1</sup> Carmichael and Klein, 2018; Di Giuseppe et al., 2009, <sup>2</sup> Murase and McBirney, 1973, <sup>3,5</sup> Kavanagh et

605 al., 2013; Rivalta et al., 2015; <sup>4</sup> Gercek, 2007, <sup>6,8,9</sup> Kavanagh et al., 2013; Rivalta et al., 2015, <sup>8</sup> Merle, 2015, <sup>10</sup>Rivalta et al., 2015, <sup>11</sup>Kennedy et al.,  
606 2018).

607

Load	Mass [kg], m	Thickness [m]	Diameter [m], $\psi$
L1	0.05	0.012	0.025
L2	0.042	0.010	0.025

608 **Supplementary Table S2:** Properties of the two cylindrical brass loads used to measure the Young's modulus.

609 **Video Figure S1:** Experimental circumferential dike formation and propagation (all videos 30  
610 frames per second): a)-b) Experiment AG-07 viewed with a) polarized light (x-z plane), and b)  
611 artificial light (y-z plane), c)-f) Experiment AG-13 (x-z plane) viewed with laser light (c), and  
612 total strain (color maps: horizontal  $E_{xx}$  (d), vertical  $E_{zz}$  (e), and shear  $E_{xz}$  (f) components) and  
613 displacement (vector arrows) calculated using digital image correlation. The red color  
614 represents extensional deformation in the normal components and anticlockwise rotational  
615 in the shear component.

616 **Video Figure S2:** Experimental cone sheet formation and propagation (experiment AG-08, 30  
617 frames per second): a) viewed with polarized light (x-z plane), and b) viewed with artificial  
618 light (y-z plane).

619 **Video Figure S3:** Experimental cone sheet formation and propagation (experiment AG-17, x-z  
620 plane, all videos 30 frames per second): a) Viewed with laser light, b)-d) total strain (color  
621 maps: horizontal  $E_{xx}$  (b), vertical  $E_{zz}$  (c), and shear  $E_{xz}$  (d) components) and displacement  
622 (vector arrows) calculated using digital image correlation. The red color represents  
623 extensional deformation in the normal components and anticlockwise rotational in the shear  
624 component.

625 **Video Figure S4:** Experimental cone sheet formation and propagation (experiment AG-19, y-z  
626 plane, all videos 30 frames per second): a) Viewed with laser light, b)-d) total strain (horizontal  
627  $E_{yy}$  (b), vertical  $E_{zz}$  (c), and shear  $E_{yz}$  (d) components) and displacement (vector arrows)  
628 calculated using digital image correlation. The red color represents extensional deformation  
629 in the normal components and anticlockwise rotational in the shear component.

630 **References:**

631

632 Anderson, E.M., 1936. The dynamics of the formation of cone-sheets, ring dykes, and  
633 caldron-subsidence. R. Soc. Edinburgh Proc. 56, 128–163.

634 doi:10.1017/S0370164600014954

635 Bagnardi, M., Amelung, F., Poland, M.P., 2013. A new model for the growth of basaltic  
636 shields based on deformation of Fernandina volcano, Galápagos Islands. Earth Planet.  
637 Sci. Lett. 377–378, 358–366. doi:10.1016/j.epsl.2013.07.016

638 Blundy, J., Mavrogenes, J., Tattitch, B., Sparks, S., Gilmer, A., 2015. Generation of porphyry  
639 copper deposits by gas-brine reaction in volcanic arcs. Nat. Geosci. 8, 235–240.

640 doi:10.1038/ngeo2351

641 Brown, D., 2012. Tracker Video Analysis and Modeling Tool for Physics Education [WWW  
642 Document]. URL <http://physlets.org/tracker/> (accessed 9.21.17).

643 Brown, D.J., Bell, B.R., 2006. Intrusion-induced uplift and mass wasting of the Palaeogene  
644 volcanic landscape of Ardnamurchan, NW Scotland. J. Geol. Soc. London. 163, 29–36.

645 doi:10.1144/0016-764905-016

646 Browning, J., Gudmundsson, A., 2015. Caldera faults capture and deflect inclined sheets: an  
647 alternative mechanism of ring dike formation. Bull. Volcanol. 77, 4. doi:10.1007/s00445-

648 014-0889-4

649 Burchardt, S., Tanner, D.C., Troll, V.R., Krumbholz, M., Gustafsson, L.E., 2011. Three-  
650 dimensional geometry of concentric intrusive sheet swarms in the Geitafell and the  
651 Dyrfjöll volcanoes, eastern Iceland. Geochemistry, Geophys. Geosystems 12, 1–21.

652 doi:10.1029/2011GC003527

653 Burchardt, S., Troll, V.R., Mathieu, L., Emeleus, H.C., Donaldson, C.H., 2013. Ardnamurchan  
654 3D cone-sheet architecture explained by a single elongate magma chamber. *Sci. Rep.* 3,  
655 1–7. doi:10.1038/srep02891

656 Burchardt, S., Walter, T.R., Tuffen, H., 2018. Growth of a Volcanic Edifice Through Plumbing  
657 System Processes—Volcanic Rift Zones, Magmatic Sheet-Intrusion Swarms and Long-  
658 Lived Conduits. *Volcan. Igneous Plumb. Syst.* 89–112. doi:10.1016/B978-0-12-809749-  
659 6.00004-2

660 Carmichael, R.S., Klein, C., 2018. Rock [WWW Document]. *Encycl. Br. inc.* URL  
661 <https://www.britannica.com/science/rock-geology> (accessed 7.26.18).

662 Chadwick, W.W., Jónsson, S., Geist, D.J., Poland, M., Johnson, D.J., Batt, S., Harpp, K.S., Ruiz,  
663 A., 2011. The May 2005 eruption of Fernandina volcano, Galápagos: The first  
664 circumferential dike intrusion observed by GPS and InSAR. *Bull. Volcanol.* 73, 679–697.  
665 doi:10.1007/s00445-010-0433-0

666 Cole, J.W., Milner, D.M., Spinks, K.D., 2005. Calderas and caldera structures: A review. *Earth-*  
667 *Science Rev.* 69, 1–26. doi:10.1016/j.earscirev.2004.06.004

668 Corbi, F., Rivalta, E., Pinel, V., Maccaferri, F., Acocella, V., 2016. Understanding the link  
669 between circumferential dikes and eruptive fissures around calderas based on  
670 numerical and analog models. *Geophys. Res. Lett.* 43, 6212–6219.  
671 doi:10.1002/2016GL068721

672 Corbi, F., Rivalta, E., Pinel, V., Maccaferri, F., Bagnardi, M., Acocella, V., 2015. How caldera  
673 collapse shapes the shallow emplacement and transfer of magma in active volcanoes.  
674 *Earth Planet. Sci. Lett.* 431, 287–293. doi:10.1016/j.epsl.2015.09.028



675 Crisp, J., 1952. The Use of Gelatin Models in Structural Analysis. Proceeding IB Inst. Mech.  
676 Eng. 12, 580–604.

677 Di Giuseppe, E., Funicello, F., Corbi, F., Ranalli, G., Mojoli, G., 2009. Gelatins as rock analogs:  
678 A systematic study of their rheological and physical properties. *Tectonophysics* 473,  
679 391–403. doi:10.1016/j.tecto.2009.03.012

680 Di Vito, M.A., Acocella, V., Aiello, G., Barra, D., Battaglia, M., Carandente, A., Del Gaudio, C.,  
681 De Vita, S., Ricciardi, G.P., Ricco, C., Scandone, R., Terrasi, F., 2016. Magma transfer at  
682 Campi Flegrei caldera (Italy) before the 1538 AD eruption. *Sci. Rep.* 6, 32245.  
683 doi:10.1038/srep32245

684 Fleet, D., Weiss, Y., 2006. Optical Flow Estimation, in: Paragios, N., and Chen, Y., and  
685 Faugeras, O. (Eds.), *Handbook of Mathematical Models in Computer Vision*. Springer  
686 US, Boston, MA, pp. 239–257. doi:10.1109/TIP.2009.2032341

687 Galland, O., Bertelsen, H.S., Eide, C.H., Guldstrand, F., Haug, Ø.T., Leanza, H.A., Mair, K.,  
688 Palma, O., Planke, S., Rabbell, O., Rogers, B., Schmiedel, T., Souche, A., Spacapan, J.B.,  
689 2018. Storage and Transport of Magma in the Layered Crust—Formation of Sills and  
690 Related Flat-Lying Intrusions, in: *Volcanic and Igneous Plumbing Systems*. pp. 113–138.

691 Galland, O., Burchardt, S., Hallot, E., Mourgues, R., Bulois, C., 2014. Dynamics of dikes versus  
692 cone sheets in volcanic systems. *J. Geophys. Res. Solid Earth* 6178–6192.  
693 doi:10.1002/2014JB011059.Received

694 Gercek, H., 2007. Poisson's ratio values for rocks. *Int. J. Rock Mech. Min. Sci.*  
695 doi:10.1016/j.ijrmms.2006.04.011

696 Geshi, N., 2005. Structural development of dike swarms controlled by the change of magma

697 supply rate: The cone sheets and parallel dike swarms of the Miocene Otoge igneous  
698 complex, Central Japan. *J. Volcanol. Geotherm. Res.* 141, 267–281.  
699 doi:10.1016/j.jvolgeores.2004.11.002

700 Gudmundsson, A., 2006. How local stresses control magma-chamber ruptures, dyke  
701 injections, and eruptions in composite volcanoes. *Earth-Science Rev.* 79, 1–31.  
702 doi:10.1016/j.earscirev.2006.06.006

703 Guldstrand, F., Burchardt, S., Hallot, E., Galland, O., 2017. Dynamics of Surface Deformation  
704 Induced by Dikes and Cone Sheets in a Cohesive Coulomb Brittle Crust. *J. Geophys. Res.*  
705 *Solid Earth* 122, 8511–8524. doi:10.1002/2017JB014346

706 Jellinek, A.M., DePaolo, D.J., 2003. A model for the origin of large silicic magma chambers:  
707 Precursors of caldera-forming eruptions. *Bull. Volcanol.* 65, 363–381.  
708 doi:10.1007/s00445-003-0277-y

709 Johnson, S.E., Paterson, S.R., Tate, M.C., 1999. Structure and emplacement history of a  
710 multiple-center, cone-sheet bearing ring complex: The Zarza Intrusive Complex, Baja  
711 California, Mexico. *Geol. Soc. Am. Bull.* 111, 607–619.

712 Kavanagh, J.L., 2018. Mechanisms of Magma Transport in the Upper Crust—Dyking. *Volcan.*  
713 *Igneous Plumb. Syst.* 55–88. doi:10.1016/B978-0-12-809749-6.00003-0

714 Kavanagh, J.L., Boutelier, D., Cruden, A.R., 2015. The mechanics of sill inception, propagation  
715 and growth: Experimental evidence for rapid reduction in magmatic overpressure. *Earth*  
716 *Planet. Sci. Lett.* 421, 117–128. doi:10.1016/j.epsl.2015.03.038

717 Kavanagh, J.L., Burns, A.J., Hilmi Hazim, S., Wood, E.P., Martin, S.A., Hignett, S., Dennis,  
718 D.J.C., 2018. Challenging dyke ascent models using novel laboratory experiments:

719 Implications for reinterpreting evidence of magma ascent and volcanism. *J. Volcanol.*  
720 *Geotherm. Res.* 354, 87–101. doi:10.1016/j.jvolgeores.2018.01.002

721 Kavanagh, J.L., Engwell, S.L., Martin, S.A., 2018. A review of laboratory and numerical  
722 modelling in volcanology. *Solid Earth* 9, 531–571. doi:10.5194/se-9-531-2018

723 Kavanagh, J.L., Menand, T., Daniels, K.A., 2013. Gelatine as a crustal analogue: Determining  
724 elastic properties for modelling magmatic intrusions. *Tectonophysics* 582, 101–111.  
725 doi:10.1016/j.tecto.2012.09.032

726 Kavanagh, J.L., Menand, T., Sparks, R.S.J., 2006. An experimental investigation of sill  
727 formation and propagation in layered elastic media. *Earth Planet. Sci. Lett.* 245, 799–  
728 813. doi:10.1016/j.epsl.2006.03.025

729 Kennedy, B.M., Holohan, E.P., Stix, J., Gravley, D.M., Davidson, J.R.J., Cole, J.W., 2018.  
730 Magma plumbing beneath collapse caldera volcanic systems. *Earth-Science Rev.* 177,  
731 404–424. doi:10.1016/j.earscirev.2017.12.002

732 Kervyn, M., Ernst, G.G.J., Van Wyk De Vries, B., Mathieu, L., Jacobs, P., 2009. Volcano load  
733 control on dyke propagation and vent distribution: Insights from analogue modeling. *J.*  
734 *Geophys. Res.* 114, 26. doi:10.1029/2008JB005653

735 Le Bas, M.J., 1987. Nephelinites and carbonatites. *Geol. Soc. London, Spec. Publ.* 30, 53–83.  
736 doi:10.1144/GSL.SP.1987.030.01.05

737 Maccaferri, F., Bonafede, M., Rivalta, E., 2011. A quantitative study of the mechanisms  
738 governing dike propagation, dike arrest and sill formation. *J. Volcanol. Geotherm. Res.*  
739 208, 39–50. doi:10.1016/j.jvolgeores.2011.09.001

740 Magee, C., Stevenson, C., O'Driscoll, B., Schofield, N., McDermott, K., 2012. An alternative  
741 emplacement model for the classic Ardnamurchan cone sheet swarm, NW Scotland,  
742 involving lateral magma supply via regional dykes. *J. Struct. Geol.* 43, 73–91.  
743 doi:10.1016/j.jsg.2012.08.004

744 Mathieu, L., Burchardt, S., Troll, V.R., Krumbholz, M., Delcamp, A., 2015. Geological  
745 constraints on the dynamic emplacement of cone-sheets - The Ardnamurchan cone-  
746 sheet swarm, NW Scotland. *J. Struct. Geol.* 80, 133–141. doi:10.1016/j.jsg.2015.08.012

747 Mathieu, L., van Wyk de Vries, B., Holohan, E.P., Troll, V.R., 2008. Dykes, cups, saucers and  
748 sills: Analogue experiments on magma intrusion into brittle rocks. *Earth Planet. Sci. Lett.*  
749 271, 1–13. doi:10.1016/J.EPSL.2008.02.020

750 McLeod, P., Tait, S., 1999. The growth of dykes from magma chambers. *J. Volcanol.*  
751 *Geotherm. Res.* 92, 231–245. doi:10.1016/S0377-0273(99)00053-0

752 Merle, O., 2015. The scaling of experiments on volcanic systems. *Front. Earth Sci.* 3, 1–15.  
753 doi:10.3389/feart.2015.00026

754 Murase, T., McBirney, A.R., 1973. Properties of some common igneous rocks and their melt  
755 at high temperatures. *Geol. Soc. Am. Bull.* 84, 3563–3592. doi:10.1130/0016-  
756 7606(1973)84%3C3563:POSCIR%3E2.0.CO;2

757 Pallister, J., Hoblitt, R., Meeker, G., 1996. Magma mixing at Mount Pinatubo: petrographic  
758 and chemical evidence from the 1991 deposits. *Fire Mud Eruptions Lahars Mt. Pinatubo*  
759 , Philipp. 1–27.

760 Pollard, D.D., Segall, P., Delaney, P.T., 1982. Formation and interpretation of dilatant echelon  
761 cracks. *Geol. Soc. Am. Bull.* 93, 1291–1303. doi:10.1130/0016-

762 7606(1982)93<1291:FAIODE>2.0.CO

763 Prejean, S., Stork, A., Ellsworth, W., Hill, D., Julian, B., 2003. High precision earthquake  
764 locations reveal seismogenic structure beneath Mammoth Mountain, California.  
765 Geophys. Res. Lett. 30. doi:10.1029/2003GL018334

766 Richey, J., Thomas, H., 1930. The Geology of Ardnamurchan, North-west Mull and Coll:  
767 Memoir for Geological Sheet 51, Part 52 (Scotland). HM Stationery Office.

768 Rivalta, E., Taisne, B., Bungler, A.P., Katz, R.F., 2015. A review of mechanical models of dike  
769 propagation: Schools of thought, results and future directions. Tectonophysics 638, 1–  
770 42. doi:10.1016/j.tecto.2014.10.003

771 Schirnick, C., Van Den Bogaard, P., Schmincke, H.U., 1999. Cone sheet formation and  
772 intrusive growth of an oceanic island-the Miocene Tejeda complex on Gran Canaria  
773 (Canary Islands). Geology 27, 207–210. doi:10.1130/0091-  
774 7613(1999)027<0207:CSFAIG>2.3.CO;2

775 Sutton, M., Wolters, W., Peters, W., Ranson, W., McNeill, S., 1983. Determination of  
776 displacements using an improved digital correlation method. Image Vis. Comput. 1,  
777 133–139. doi:10.1016/0262-8856(83)90064-1

778 Taisne, B., Tait, S., 2009. Eruption versus intrusion? arrest of propagation of constant  
779 volume, buoyant, liquid-filled cracks in an elastic, brittle host. J. Geophys. Res. Solid  
780 Earth 114, B06202. doi:10.1029/2009JB006297

781 Takada, A., 1990. Experimental study on propagation of liquid-filled crack in gelatin: Shape  
782 and velocity in hydrostatic stress condition. J. Geophys. Res. 95, 8471.  
783 doi:10.1029/JB095iB06p08471

784 Troll, V.R., Emeleus, C.H., Donaldson, C.H., 2000. Caldera formation in the Rum Central  
785 Igneous Complex, Scotland. *Bull. Volcanol.* 62, 301–317. doi:10.1007/s004450000099

786 USGS, H.V.O., 2018. Preliminary Analysis of the ongoing Lower East Rift Zone ( LERZ )  
787 eruption of Kīlauea Volcano : Fissure 8 Prognosis and Ongoing Hazards.

788 Watanabe, T., Masuyama, T., Nagaoka, K., Tahara, T., 2002. Analog experiments on magma-  
789 filled cracks : Competition between external stresses and internal pressure. *Earth*  
790 *Planets Sp.* 54, 1247–1261. doi:10.1186/BF03352453

791